Fall 2013

Experimental measurements of a two phase surface jet

Matias Nicholas Perret
University of Iowa

EXPERIMENTAL MEASUREMENTS OF A TWO PHASE SURFACE JET

by

Matias Nicholas Perret

A thesis submitted in partial fulfillment
of the requirements for the Master of
Science degree in Mechanical Engineering
in the Graduate College of
The University of Iowa

December 2013

Thesis Supervisor: Associate Professor Pablo M. Carrica

Graduate College
The University of Iowa
Iowa City, Iowa

CERTIFICATE OF APPROVAL

_____

MASTER'S THESIS

_____

This is to certify that the Master's thesis of

Matias Nicholas Perret

has been approved by the Examining Committee
for the thesis requirement for the Master of Science
degree in Mechanical Engineering at the December 2013 graduation.

Thesis Committee: _____
Pablo M. Carrica, Thesis Supervisor

_____
Christoph Beckermann

_____
James H. J. Buchholz

_____
Albert Ratner

ACKNOWLEDGMENTS

First and foremost, I would like to thank my advisor, Pablo Carrica. Thank you, Pablo, for your guidance, support and enthusiasm you have given me through my graduate career.

I would also like to thank Christoph Beckermann, James H. J. Buchholz and Albert Ratner for their willingness to serve on my thesis committee. I want to acknowledge the work of Marcela Politano and Mehdi Esmaeilpour who have helped along the way in completing this project. I would also like to recognize Geb Thomas, for his continual open-minded mentoring throughout my undergraduate and graduate career. Additional thanks must also be extended to Albert Ratner for generously donating the use of his high speed camera, as well as James H.J. Buchholz and Craig J. Wojcik for sharing their expertise in PIV measurements, Greg Wagner and Doug Houser for their help with our LDV setup and finally Tim Houser, Brandon Barquist and the rest of the IIHR shop staff for lending a helping hand whenever one was needed.

This work was partially supported by the National Science Foundation Fluid Dynamics Program, grant number 0853286, with Dr. Horst Henning Winter as program manager.

ABSTRACT

The effects of bubbles on a jet issued below and parallel to a free surface are experimentally studied. The jet under study is isothermal and in fresh water, with air injectors that allow variation of the inlet air volume fraction for 0% to 13%. Measurements of the jet exit conditions, water velocity, water entrainment, Reynolds stresses and surface currents have been performed using LDV, PIV and surface PIV. Air volume fraction, bubble velocity, chord length and free surface elevation and RMS have been obtained using local phase detection probes. Visualization was performed using laser-induced fluorescence. Measurements show that water entrainment decreases up to 22% with the presence of bubbles, but surface current strength increases up to 60% with 0.4 l/min of air injection. The mean free surface elevation and turbulent fluctuation significantly increase with the injection of air. The water normal Reynolds stresses are damped by the presence of bubbles in the bulk of the liquid, but very close to the free surface the effect is reversed and the normal Reynolds stresses increase slightly for the bubbly flow. Flow visualizations show that the two-phase jet is lifted with the presence of bubbles and attaches to the free surface sooner. Significant bubble coalescence is observed, leading to an increase of 20% in mean bubble size as the jet develops. The coalescence near the free surface is particularly strong, due to the time it takes the bubbles to pierce the free surface, resulting in a considerable increase in the local air volume fraction.

TABLE OF CONTENTS

LIST OF TABLES

LIST OF FIGURES

LIST OF SYMBOLS

Q_w	Water volumetric flow rate
Q_a	Air volumetric flow rate
j_w	Superficial water velocity
j_a	Superficial air velocity
$U_{0,w}$	Reference water velocity
U_{RMS}	Velocity fluctuation about the mean velocity
k	Turbulent kinetic energy
$< u'u' >$	Axial Reynolds stress
$< w'w' >$	Vertical Reynolds stress
$< u'w' >$	Shear Reynolds stress
ζ	Free surface elevation
α	Void fraction
C_l	Bubble chord length
U_{tof}	Bubble velocity

CHAPTER 1: INTRODUCTION

Surface jets are jets issued horizontally, parallel and close to a free surface. Free surface constrained jets differ from wall constrained jets in that the free surface can deform and that the tangential stresses are essentially zero. Besides having these two inherently interesting properties, they appear with some frequency in nature and in engineering processes. Two examples of interest are spillway jets on hydropower dams retrofitted with deflectors and waterjet powered ships. In particular, spillway jets are of great relevance because they have significant environmental impact. Note that in these examples the jets carry bubbles and therefore are multiphase surface jets.

1.1 Motivation

As an example of the importance of advancing the understanding of two-phase surface jets, the case of the flow in the tailrace of a dam is discussed. Bubble gas disease in fish, caused by high concentrations of total dissolved gas (TDG), has been known to be detrimental, or even lethal to fish [1]. In an effort to minimize the supersaturation of total dissolved gas, spillway deflectors have been installed throughout the US portion of the Columbia and Snake River basins. Deflectors act to redirect plunging water horizontally forming a bubbly surface jet that prevents the bubbles from plunging to depth in the stilling basin, thus reducing the air dissolution. It has been demonstrated that the surface jets cause a significant change of the flow pattern since they attract water toward the jet region, a phenomena called water entrainment. This entrainment leads to mixing, modifying the gas distribution and TDF concentration field. The Wanapum and McNary Dams on the Columbia River are good examples with field measurements of velocity before and after deflectors were installed. Model scale experiments and single-phase models cannot capture the strong water entrainment observed in the field or large-scale model experiments [2, 3]. It is conjectured that this is due to the bubbly flow present on field scale, not captured by small model scale experiments or single-phase computational

models. A deeper understanding of bubbly surface jets would help proper modeling of the phenomenon, which would allow for the design of better mitigation measures for TDG, ultimately leading to increased fish survival.

The objective of this thesis is to extend the previous research on surface jets to analyze the case in which bubbles are introduced with the jet. The study was entirely experimental, and aims to provide fundamental insights into how the bubbles interact with the jet as it evolves, how the jet is affected by the presence of bubbles, how the free surface is affected by the presence of bubbles, how the surface currents are affected by the presence of bubbles, and how the water entrainment is affected by bubbles.

1.2 Background

Single-phase water surface jets have been the subject of study for some time, mostly experimentally [4, 5, 6, 7, 8, 9] but also numerically [10, 11] and theoretically [12]. These studies have primarily focused on the analysis of the differences between classic free jets [13] and jets confined by a free surface, reporting turbulence and velocity distributions, as well as free surface deflection, jet attachment to the free surface, and water entrainment. Most of the work was motivated by the study of surface ship wakes.

Early observations through visualization of single-phase surface jets show that the presence of the free surface greatly modifies the structure of the jet [4]. The free surface responds strongly to the large-scale structures of the jet creating surface disturbances that propagate away from the jet axis. A wide range of wavelengths as well as vorticity normal to the free surface detected as “dimples” are observed in the shadowgraph visualizations [7, 8, 14]. Leipmann [4] performed an experimental investigation to study the near flow field and entrainment due to axisymmetric cylindrical surface jets, very near the surface. He reported that the jet curved toward the free surface, and attributed this to the Coanda effect also observed on wall-bounded flows [15]. Another observed phenomenon was the development of streamwise vortices, which were generated by

interaction of the vortex rings around the core of the jet with the free surface. This streamwise vorticity was explained by the author as tilting of the vortex rings due to interaction with its image across the free surface. The generation of streamwise vorticity plays an important role on entrainment and mixing. Anthony and Willmarth [5] performed experiments with a turbulent jet issuing from a circular nozzle beneath and parallel to a free surface, with distances from the free surface deep enough such that the jet is fully turbulent before it interacts with the free surface. Their 3D laser Doppler velocimeter (LDV) measurements revealed that near the jet's center-plane the interaction between the jet and the free surface is most intense and the velocity fluctuations normal to the free surface decrease approaching the interface, while the tangential fluctuations increase, similar also with wall-constrained jets [16]. This type of behavior is expected and is due to the no penetration condition at the free surface. Liepmann [4], Antony and Willmarth [5] also found that the jet is attracted toward the free surface, and that streamwise vorticity was generated. They attribute this vorticity to the presence of Reynolds stress gradients. This type of behavior can also be seen in a jet discharging parallel to a solid wall. The similarity between these two constrained jets is the presence of a boundary at which the normal velocity must vanish. Madnia and Bernal [7] used single-component hot-film measurements and flow visualization to study a round surface jet. They observed that surface waves developed when the jet first interacted with the free surface. These essentially plane waves propagated away from the jet axis.

The Anthony and Willmarth [5] study also shows evidence of the presence of surface currents, a thin layer of flow away from the jet axis very near the free surface. This phenomenon was also observed by Walker and Johnston [17] and Hoekstra [18] in the wake of model ships, and later confirmed by Walker *et al.* [8] for surface jets under a wider set of conditions. Surface currents were later described by Walker [12] as a result from the imbalance between the lateral gradients in the $\overline{v^2}$ and $\overline{w^2}$ Reynolds stresses. As originally found by Anthony and Willmarth [5], near the free surface $\overline{w^2}$ decreases, and

$\overline{v^2}$ increases, thus creating the surface currents. Walker *et al.* [8] used a similar experimental setup as [5] varying the Reynolds number from 12,700 to 102,000 for *Fr* = 1 and the Froude number from 1 to 8 for *Re* = 12,700. They measured all six Reynolds stresses and three mean velocity components at two cross sectional planes using three-component LDV. They show that there is a direct relation between the generation of the surface current by the streamwise vorticity with the decrease of surface normal velocity fluctuations and the corresponding increase in tangential velocity fluctuations. Higher Froude numbers resulted in a transfer of energy to free surface fluctuations, which reduced the surface current. A higher Reynolds number shows a slower decay of tangential vorticity. A larger jet has been studied by Trujillo *et al.* [9] for *Re* = 3.41 10^6 and *Fr* = 4.7. They also performed numerical studies using Reynolds-averaged Navier Stokes (RANS) and large eddy simulation (LES). Through they obtained good agreement between numerical simulations and experiments, their jet does not reach the surface jet regime, behaving mostly as a free jet.

Entrainment by axisymmetric jets has been studied since the pioneering works of Morton *et al.* [19], Townsend [20] and Wygnanski and Fiedler [13]. The near-field entrainment in axisymmetric jets has been studied by Liepmann and Gharib [22] using particle image velocimetry (PIV). The authors focused on the formation and growth of streamwise vorticity and its effect on entrainment, finding that streamwise vorticity produces much more entrainment than azimuthal vorticity. In a later work, Liepmann and Gharib [6] studied the entrainment of a surface jet, reporting also the surface currents observed by Anthony and Willmarth [5] and Walker *et al.* [8]. They found that the entrainment peaks at a certain distance downstream of the jet exit, closer to the jet exit as the jet axis gets closer to the free surface. This is opposed to the entrainment observed on unconfined jets, where the entrainment increases with the distance from the jet exit and then levels off. More recently, Baddour *et al*. [21] studied entrainment by a planar surface jet measuring core axial velocities with LDV. They focus on obtaining entrainment

coefficient as defined by Morton *et al.* [19] and the entrainment constant of Townsend [20], finding that the representation of entrainment using an entrainment coefficient holds well for the total entrainment coefficient, but noticed that the vertical entrainment coefficient is strongly dependent on cross currents.

Upward issuing vertical [23, 24, 25] and horizontal [26] bubbly jets have been studied to some extent, there is a lack of studies on bubbly jets interacting with a free surface. Sun and Faeth [23] concentrated on the analysis of the air phase for diluted flows. Though a small increase in the turbulent kinetic energy was found when bubbles greater than 1 mm in diameter were injected, no lateral velocities were reported, so the jet-induced water entrainment could not be quantified. Lima Neto *et al.* [26] measured slip velocity, air volume fraction and bubble size distribution for a geometry similar to Sun and Faeth [23]. They also studied a horizontal jet deep below a free surface [26], concentrating in the evaluation of the two-phase properties of the flow and applicability to aerators and mixers.

CHAPTER 2: EXPERIMENTAL CONSIDERATIONS

The experiment was designed with the goal of controlling the parameters that influence the results as tightly as possible. The purpose was to guarantee repeatability as a variety of instruments are used to measure different aspects of the flow. To achieve this, the water of the facility was filtered continuously and changed frequently, while the temperature of the water was maintained fixed with a controller. Details of the facility, in instrumentation and procedures used are described below.

2.1 Flume Facility

The experimental set-up consisted of a $4\text{ m} \times 0.75\text{ m} \times 0.75\text{ m}$ flume made of 12 mm plate glass on the sides and bottom supported by a steel frame, see Figure 1. The flume was fitted with a constant head ($0.75\text{ m} \times 0.75\text{ m} \times 0.75\text{ m}$) tank to feed the jet and an overflow tank ($0.6\text{ m} \times 0.6\text{ m} \times 0.6\text{ m}$) to maintain a constant free surface elevation. Maintaining these two levels fixed ensured a constant pressure difference, which resulted in a stable flow rate through the jet. Water was forced by means of a 750 W pump through two 20 micron particulate filters mounted in series between the overflow tank and the constant head tank. Excess water from the constant head tank was discharged to the overflow tank. The water flow rate was monitored using a calibrated rotameter (Dwyer VA10417).

Air was supplied from a large air compressor, and was filtered through particulate and moisture filters prior to passing through a pressure regulator and a needle valve to control the flow rate. The flow rate was monitored using an Omega FMA31000 series mass flow meter. The temperature of the air, originally coming from outside the room, was maintained at the same temperature of the water by passing through an aluminum heat exchanger submerged in the bulk of the flume.

The temperature of the water was maintained at 25° C using two 4 kW stainless steel heating elements located on each end of the flume. In addition, the room

temperature was also maintained at 25° C to minimize heat losses from the tank. Since the experiment was installed inside the highly insulated ice room at IIHR- Hydroscience and Engineering, The University of Iowa, originally designed for arctic environment experiments, the room temperature was easy to control and very stable. Three K-type thermocouples in stainless steel sheaths, one located in the constant head tank and two in the flume, fed to an Omega CN7200 PID controller that controlled two solid-state relays connected to the heating elements. The temperature controller inside the tank was disabled during experiments to avoid natural convection currents, and enabled in between experiments to maintain the desired experimental conditions.

A 3-axis traverse system was used for positioning the LDV and optical probes as well as the jet for PIV measurements. Each axis was supported with Thomson linear bearings on linear rails and was equipped with ½"-10 tpi ACME lead screws with anti-backlash nuts. NEMA 34 shell stepper motors were used in conjuncture with GECKO drivers to drive the lead screws and provide linear motion allowing for both continuous and discreet probe positioning. This combination allowed for a positional accuracy of less than 0.075% over the full range of motion. Parallelism and trueness of the traverse relative to the free surface was measured using the optical probes and traversing to the free surface at various points throughout the measuring domain. Along the longitudinal direction (x-axis) the deviation of the traverse to the free surface was less than 2.5 μm over the measurement domain and 65 μm in the transverse direction (y-axis).

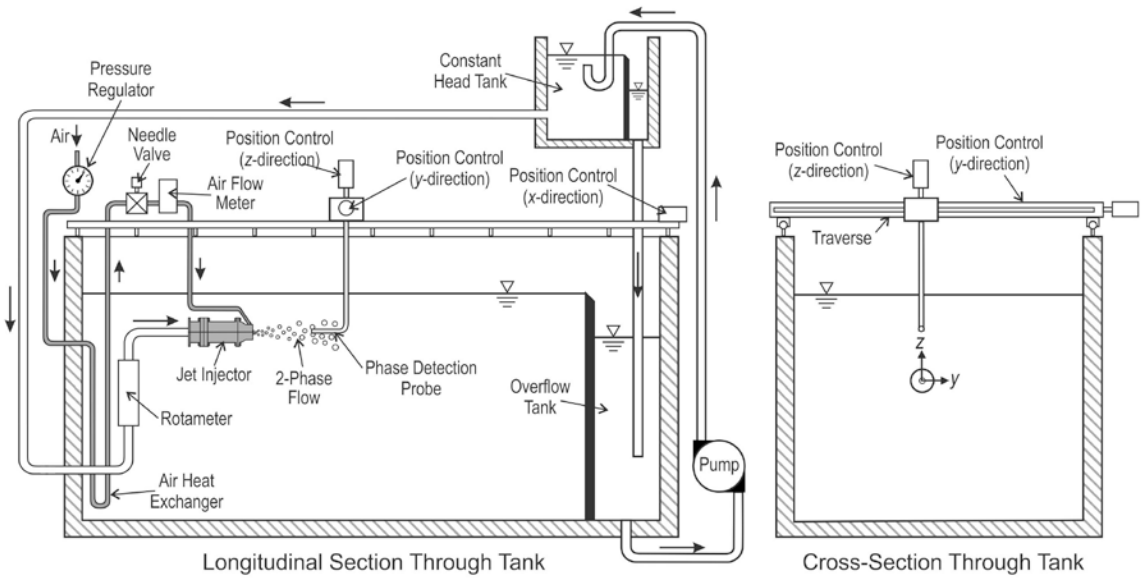

Figure 1: Experimental flume set-up.

2.2 Jet and bubble injector

The jet injector was made of clear acrylic plastic with an aluminum nozzle. The intake of the jet, fed by the constant head tank, was a 25.4 mm flange style fitting followed by a Venturi contraction and expansion prior to the jet nozzle. The jet nozzle, made of 7005 Aluminum, follows a 5th-order parabola such that the inlet and exit section have zero first and second derivatives, with an exit diameter $d = 6.35$ mm. The corresponding equation for the radius is, as defined by the author, $r = -5.4056 \times 10^{-6}x^5 + 3.4326 \times 10^{-4}x^4 - 5.8125 \times 10^{-3}x^3 + 12.7$, with r in mm and x the axial position running from 0 to 25.4 mm. As Figure 2 shows, air was injected through six 32 gauge (150 µm ID) hypodermic stainless steel tubes spaced equidistantly around the perimeter of the jet exit. A plenum on the perimeter of the exit of the jet supplied air to the hypo tubes and was sealed with a precision fine thread. The air injected into the plenum was pushed through the hypo tubes where bubbles form and are carried through by the flowing water at the jet exit. This allowed for uniform bubble distribution at the exit of the jet with the bubbles having minimal size. The contraction ratio of the Venturi

along with the hypo tube diameter could allow for a certain extent of control over the bubble size, which we looked to minimize. The jet coordinate axis (Figure 3) is zeroed at the exit of the jet along the centerline of the jet, with all measurement locations taken relative to this coordinate system.

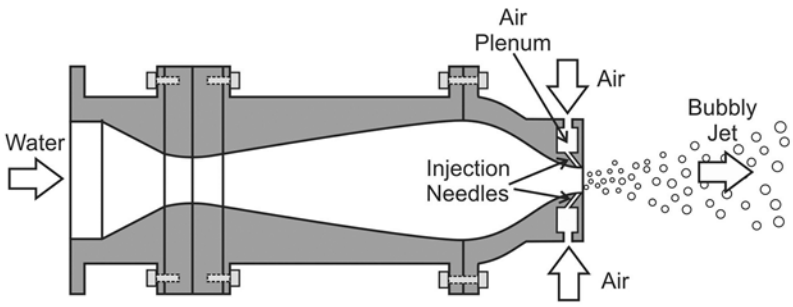

Figure 2: Jet nozzle and air injector.

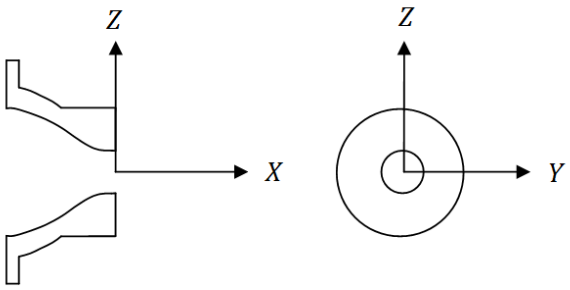

Figure 3: Jet coordinate axis, side view (left) and front view (right).

2.3 Particle image velocimeter

PIV measurements were obtained using a LaVision Flowmaster stereo system. The system consisted of two Image ProX 2048×2048 pixel dual CCD cameras with a Litron 200 mJ/pulse neodymium-doped yttrium aluminum garnet (Nd:YAG) laser with a 532 nm wavelength and fitted with sheet optics. The laser sheet thickness was set to 1.5

mm. Each camera was fitted with Scheimpflug adapters mounted to the 105 mm Nikon lenses used. For the characterization of the jet exit, extension tube sets were used in conjunction with the Scheimpflug adapters to maintain adequate focus. Seeding with 10 μm rhodamine B fluorescent particles with fluorescence color in the 560~584 nm range was necessary to avoid saturation of the CCD cameras. These seed particles were developed by Pedocchi *et al.* [27], and at 10 μm have a terminal velocity of 0.04 mm/s, much slower than the slowest velocities measured in the experiment and beyond the dynamic range of the PIV as used in this work. 540 nm low-pass filters were used to filter out any reflections of the laser to the cameras, especially from the bubbles in the flow. To minimize refraction errors, two water filled prisms were fitted directly to the flume for the cameras to look through, see Figure 4. Timing and data acquisition was carried out by the LaVision DaVis 8.1 software. Calibration, image processing and post-processing was carried out with the same software. The CCD cameras were calibrated using a custom CNC machined dual level calibration plate for characterizing the jet exit and a LaVision #20 calibration plate for the far field measurements. The DaVis software was used to fit a third order polynomial to de-warp the camera image to the regular grid of the calibration target. The error of the fit, which is a contributing factor to the PIV uncertainty, is summed up in the RMS-fit error, which is a value of the average deviation of the de-warped mark position to the ideal regular grid. A disparity map from a set of particle images from both cameras was computed in the self-calibration mode of DaVis to correct for misalignment of the laser light sheet to the calibration plane. Image processing to compute velocity vectors was carried out using a standard cross-correlation with multiple passes per window (64 x 64 pixels for the far field, 128 x 128 pixels for the jet exit) using a 50% overlap with a median filter employed to remove outliers.

The systems dynamic range was not able to handle the velocity differences between the jet core and the far field, and thus the time between PIV images was optimized to measure the far field, which caused a poor correlation at the core of the jet.

For the chosen time between frames, optimized for the far-field flow, the seeding particles observed in the first image in the jet core leave the light sheet before the second image is taken. Mean velocity convergence was ensured by taking 1,000 images per plane of interest at 7 fps. For characterizing the jet exit, 10,000 images at a rate of 0.15 Hz were taken to allow for mean turbulent quantities to converge. For the PIV measurements, the traverse system described in 2.1 was used to position the jet with respect to the laser light sheet. This was done to avoid refocusing and calibration every time a new jet position was used. Uncertainty analysis was carried out following the Recommended Procedures and Guidelines set by the ITTC [28].

2.4 Surface PIV

The surface PIV measurements were performed using specially manufactured rhodamine B floating particles with specific density 0.8 and a diameter of 0.75 mm. The particles were made with a two part urethane plastic mixed with rhodamine B dye and fumed silica. The plastic was ground and sieved, using particles between the U.S. standard screen sizes 20 (0.85mm) and 30 (0.6mm). The choice of the particle diameter is a trade-off between available light and resolution of the camera in one hand, and minimization of intrusivity on the other hand, so the particles where manufactured to the smallest size that provided good contrast in the images. A 1280x1024 X-StreamVision XS-3i high speed camera, fitted with a 105 mm Nikon lens and 540 nm low-pass filter, was used to capture single exposed particle images of the free surface at a frame rate of 400 Hz. Illumination was provided from a Laserglow Technologies 10 watt 532 nm solid state laser fitted with a spherical lens, illuminating the free surface from above. Image processing was carried out using the same DaVis 8.1 software. Surface PIV measurements were done with the jet aligned to the long axis of the flume and thus reached out to $x/d = 32$.

2.5 Laser Doppler velocimeter

LDV velocity measurements were obtained using a TSI system. The system used a Coherent Innova 70 Argon Ion laser. A TSI ColorBurst Multicolor Beam Separator, Model 9201, separated the 514 nm and 488 nm laser colors used to measure velocities in the streamwise and vertical directions, respectively. Shifted and un-shifted beams were generated using a Bragg cell controlled by an IFA 655 signal processor. Frequency shifts of 500 kHz for the streamwise direction and 200 kHz for the vertical direction were used to discern negative from positive velocities. The beams were coupled with fiber optics to

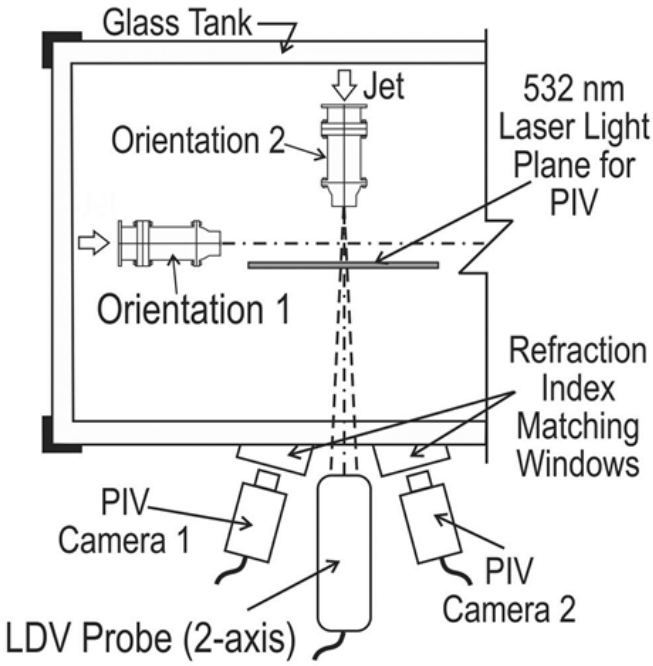

Figure 4: PIV and LDV arrangements.

a 350 mm TSI 2-component probe with the receiving optics going to ColorLink Plus multicolor receiver, model 9230, and to the IFA 655. The software FIND for windows

was used for all control and data acquisition. Seeding with 5 μm glass particles was necessary to get adequate data sampling rate. Calibration was performed against a submerged rotating wheel of known diameter and rotational speed.

The effects of bubbles on the LDV signal, for the bubble sizes observed in this experiment (0.5~2.5 mm in diameter), are a decrease in the data rate due to less probable simultaneous beam penetration to the measurement volume and invalid signals when a bubble is in the measurement volume. Large bubbles return much stronger signal, and can be filtered by using threshold rejection [29]. However, as discussed in Mudde *et al.* [30], threshold rejection does not change results much since the bubbles do not contribute significantly to the data rate. In addition, dense seeding greatly increases the data events in the liquid phase making accepted bubble detections negligible. Other methods to filter the raw signals, such as velocity filtering, are not applicable for flows with very similar bubble and liquid velocities as in this work. Mudde *et al.* [30] proved that though the data rate is dramatically decreased for bubbly flows, the LDV system measures essentially the liquid velocity if the seeding is dense.

Since measurement of cross-correlations was a goal and the data rate was too small to use random mode to compute cross-correlations with confidence, the coincidence measurement mode was used, thus resulting in a very low data rate and long measurement times at each point where the air volume fraction was high, in some cases as low as 10 Hz. Uncertainty analysis was carried out as per the guidelines of the ITTC Guidelines and Recommendations [31]. Errors due to uncertainty in wavelength and Doppler frequency were considered negligible, with the primary errors being from calibration. The rotating wheel used for calibration was controlled by a DC-power supply and monitored with an optical encoder. The eccentricity of the wheel was measured using a Fowler dial test indicator. Both channels of the LDV system were calibrated against the rotating wheel and the resulting instrumental uncertainty in velocity was found to be

1.053 mm/s. In addition, statistical errors were considered resulting in the uncertainties shown in the velocity results.

2.6 Phase detection probe

A specifically designed optical local phase detection probe was developed for the purpose of this experiment. The principle of operation is based on the different indexes of refraction of water and air. An infrared light is sent through a fiber optics cable to the probe tip, and depending on which phase the fiber tip is in the intensity of the light reflected back from the tip varies, which allows reconstruction of the phase indicator function [32, 33]. This process was carried out with RBI (Meylan, France) infrared optoelectronic modules, which convert the analog signal into a digital signal with a double threshold technique, resulting in detection of bubble interfaces with resolution of approximately 1 μs.

Phase detection probes measure the air phase indicator function, defined as [32]:

$$\chi(\mathbf{r},t)=\begin{cases}1 & if\ the\ probe\ tip\ is\ in\ air\\ 0 & if\ the\ probe\ tip\ is\ in\ water\end{cases} \quad (1)$$

Details on how the indicator function is obtained from the analog signals measured from the probe, and how filters are applied to remove from the signal the events in which the probe is out of the free surface are discussed in Johansen *et al*. [33]. In Johansen *et al*. [33] there is also detailed discussion on how the air volume fraction, the bubble velocity and the bubble size distribution, as well as how to estimate uncertainty on the measurements. The reader is referred to that reference and only the basic fundamentals of the probe are discussed herein.

A double tip probe measures the indicator function at two points at a distance L apart and can compute the velocity (Equation 3) of individual bubbles by measuring the

time of flight of the air/water interfaces between the known distance from one probe tip to the second. The cord length (Equation 4) of each bubble is measured using the bubble velocity and the residence time in air for each bubble as seen by the individual probe tip. Note that the chord length does not represent the bubble diameter, as a bubble can be pierced in any location, yielding a chord length that could be less than or equal to but never exceeding the bubble diameter. The chord length gives insight as to whether bubbles are coalescing or breaking up. Assuming that the bubbles are spherical, a bubble size distribution can also be obtained from a chord length distribution.

$$U_{tof,i} = \frac{L}{t2_i - t1_i} \quad (2)$$

$$C_l = \Delta t_i U_{tof,i} \quad (3)$$

To accurately detect bubbles on the order of 50 μm size, and to achieve good cross correlation between the two tips of the probe, a probe was developed and manufactured by the author to have an effective tip diameter on the order of 20 μm. To achieve these small diameters while maintaining enough strength in the tips, 125 μm sapphire fibers, made by Micromaterials Inc., were polished to a double angle, see Figure 5. The primary angle, 5^o axisymmetric, reduces the effective diameter of the sapphire fiber from 125 μm to 20 μm. The second angle at the tip is 45^o. This allows for maximum amount of light reflected back. Each sapphire tip is matted to a $100/140$ μm core/cladding diameter glass fiber optic cable using a refraction index matching gel. The probes were mounted with the vector joining the probe tips aligned to the axis of the jet.

From the indicator function, the time-averaged air volume fraction is computed from:

$$\alpha(\mathbf{r}) = \frac{1}{T}\int_0^T \chi(\mathbf{r},\tau)d\tau \quad (4)$$

where T is the averaging period. T has to be long enough such that the air volume fraction converges to a steady value. Following Carrica *et al*. [34], this means that enough bubbles are measured and that the integration time is significantly longer than the characteristic time of whatever transient physical process is occurring in the two-phase flow. For convergence of other variables, such as the bubble size distribution, significantly longer times are needed. In this work, measurement times range from 1 to 20 minutes. In most conditions several measurements were taken to check repeatability and to reduce statistical errors.

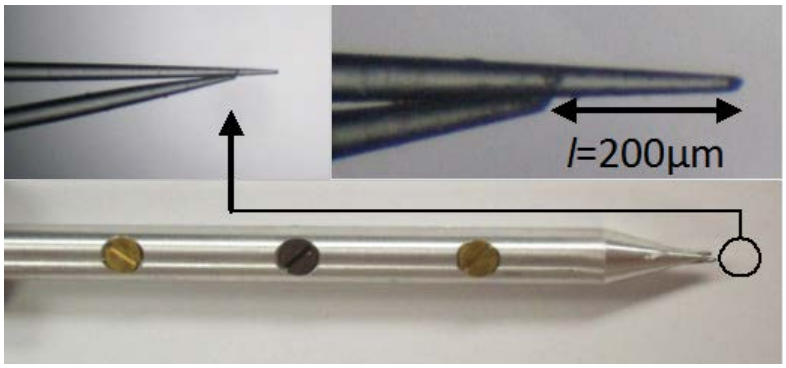

Figure 5: Optical phase-detection probe and details of the tip.

2.7 Flow visualization

Flow visualization was performed using the laser induced fluorescence (LIF) technique, injecting Rhodamine B fluorescent dye illuminated with a 532 nm wavelength solid state laser (Laserglow LRS-0532-TFW10000-10, 10 W). The laser produced a light sheet 2 mm thick. A Nikon D80 still camera was used to take images. High speed video was taken using an IDT X-Stream XS-3 camera with up to 1260 x 1024 pixels of

resolution and a frame trate of up to 1440 frames/s at 1260 x 448 pixels. In all cases a 540 nm low-pass filter was used to filter out the green light from the laser.

2.8 Experimental procedure and conditions

Experiments included various water and air flow rates as described in Table 1. For all cases, the jet axis was positioned at a depth h = 2d below the free surface. The baseline Case 0 in Table 1 has a volumetric flow rate of $Q_w = 3.41$ l/min and air volumetric flow rate $Q_a = 0$ l/min, corresponding to an average water velocity of $U_{0,w} = 1.795$ m/s. These conditions result in $Re = U_{0,w}d/\nu = 13080$ and $Fr = U_{0,w}/\sqrt{gd} = 7.21$, and are close to those used by Walker *et al.* [5] for their smallest jet ($Re = 12700$, $Fr = 8.0$).

Two strategies were followed to study the effects of air bubbles on the jet. The first strategy was to maintain the volumetric flow rate of water constant and increase the volumetric flow rate of air up to $Q_a = 0.4$ l/min, which corresponds to a superficial velocity of air $j_a = 0.21$ m/s. Assuming no slip between the phases, this corresponds to an air volume fraction $\alpha = 10.5\%$. Under this strategy the momentum of the jet increases slightly with respect to the single phase jet, because the liquid velocity will increase. Again, assuming no slip between the phases [35],

$$U_w = \frac{j_w}{(1-\alpha)} = 2 \text{ m/s} \qquad (5)$$

increasing the axial momentum by approximately 11.2% respect to baseline Case 0. Cases 1 and 2, shown in Table 1, follow this strategy.

The second strategy involved maintaining the total volumetric flow rate constant, and is represented by Case 3 in Table 1. Under this condition, the liquid exit velocity is the same as the single-phase jet, but the total momentum decreases. Neglecting the

momentum of the air and assuming no slip between the phases at injection, the momentum of the jet is 81% of the momentum of the single-phase jet in baseline Case 0.

Velocities inside the jet core were measured using the LDV system. Measurements were taken axial locations $x/d = 8, 16, 24, 32$ and at the planes $y/d = 0$ and $z/d = 1.6$. Bubble velocity and volume fraction measurements were taken in $Y - Z$ planes at 7 locations downstream of the jet exit, $x/d = 2, 4, 8, 12, 16, 24$ and 32. Measurements were taken only in the positive *Y*-direction. Symmetry compliance was checked at $x/d = 8$, finding that the flow exhibited a high level of symmetry. Each point was measured for at least 5 minutes, longer in regions of very low void fraction. To determine the bubble size distribution, measurements were taken at a single depth for 20 minutes, since more statistics are needed to obtain good quality results. Errors in two-phase flow results can occur when the probes come out of the water as a result of free surface oscillations. These appear in the signal as long times in air (compared to the bubbles that have much shorter residence times). To prevent this problem a variety of filters were used on the post-processing step, as described in Johansen *et al.* [33]. General data analysis to obtain bubble velocities and size distribution as well as uncertainty estimations followed also the techniques presented in Johansen *et al.* [33].

The PIV system was used to measure the velocity outside the jet core and the mean velocity and turbulence at the jet exit. Surface currents were measured with the surface PIV and finally, the free surface elevation was also measured using the local phase-detection probe. Details of the novel technique are described in section 3.2.6.

Table 1: Experimental conditions.

	Water Flow Rate (l/min)	Air Flow Rate (l/min)	Combined Flow Rate (l/min)
Case 0	3.41	0	3.41
Case 1	3.41	0.4	3.81
Case 2	3.41	0.2	3.61
Case 3	3.069	0.341	3.41

CHAPTER 3: RESULTS AND DISCUSSION

The results are broken up into three sections: flow visualizations (3.1), liquid measurements (3.2) and two-phase measurements (3.3). All subsequent plots are showed in with non-dimensional units unless otherwise noted. The principal axes (x – axial, y – transversal and z – vertical), are non-dimensionalized using the jet diameter $d = 6.35$ mm, while velocities and relevant quantities are non-dimensionalized using the average water velocity, defined in 2.8, $U_{0,w} = 1.795$ m/s.

3.1 Flow visualizations

Two conditions were studied with $Q_w = 3.41$ l/min, the baseline Case 0 with $Q_a = 0$ l/min and the high air flow rate Case 1 with $Q_a = 0.4$ l/min.

Figure 5 and Figure 6 show long and short exposure views of the jet on the center plane $y/d = 0$ without and with air being injected, respectively. The visualization shows that the two-phase jet is lifted by the presence of bubbles and reaches the free surface sooner. This is also clearly seen in the axial cross sectional views at $x/d = 32$ shown in Figure 7.

Figure 8 (long exposure) and Figure 9 (short exposure, 250 μs). The lateral spread of the injected dye near the free surface observed in these figures also shows that the bubbly jet produces more lateral velocities near the interface (the surface currents observed by Anthony and Willmarth [5], and others) than the single-phase surface jet. The lateral spread can also be seen in Figure 10, which shows a view from the top of the free surface. Figure 10 also shows that the interaction of the jet fluid with the free surface occurs intermittently as the jet fluid breaks into vortices. In addition, the jet spreads less downward and vortex filaments are smaller when bubbles are present. This is consistent with the reduction of the negative vertical velocity by the presence of the bubbles. Noticeable is the increment of bubble size as bubbles move away from the jet core and at the free surface.

The instantaneous views in Figure 9 expose the size of the turbulent scales produced by the decay of the jet. Note that some of the turbulent eddies are smaller than the injected bubbles. Notice also that in Figure 9 that some small bubbles are still present deep away from the free surface, but higher up bubbles are considerably larger. Also, as bubbles are attached to the free surface, they become considerably larger due to coalescence and result in the observed higher air volume fraction, as discussed in 3.3.

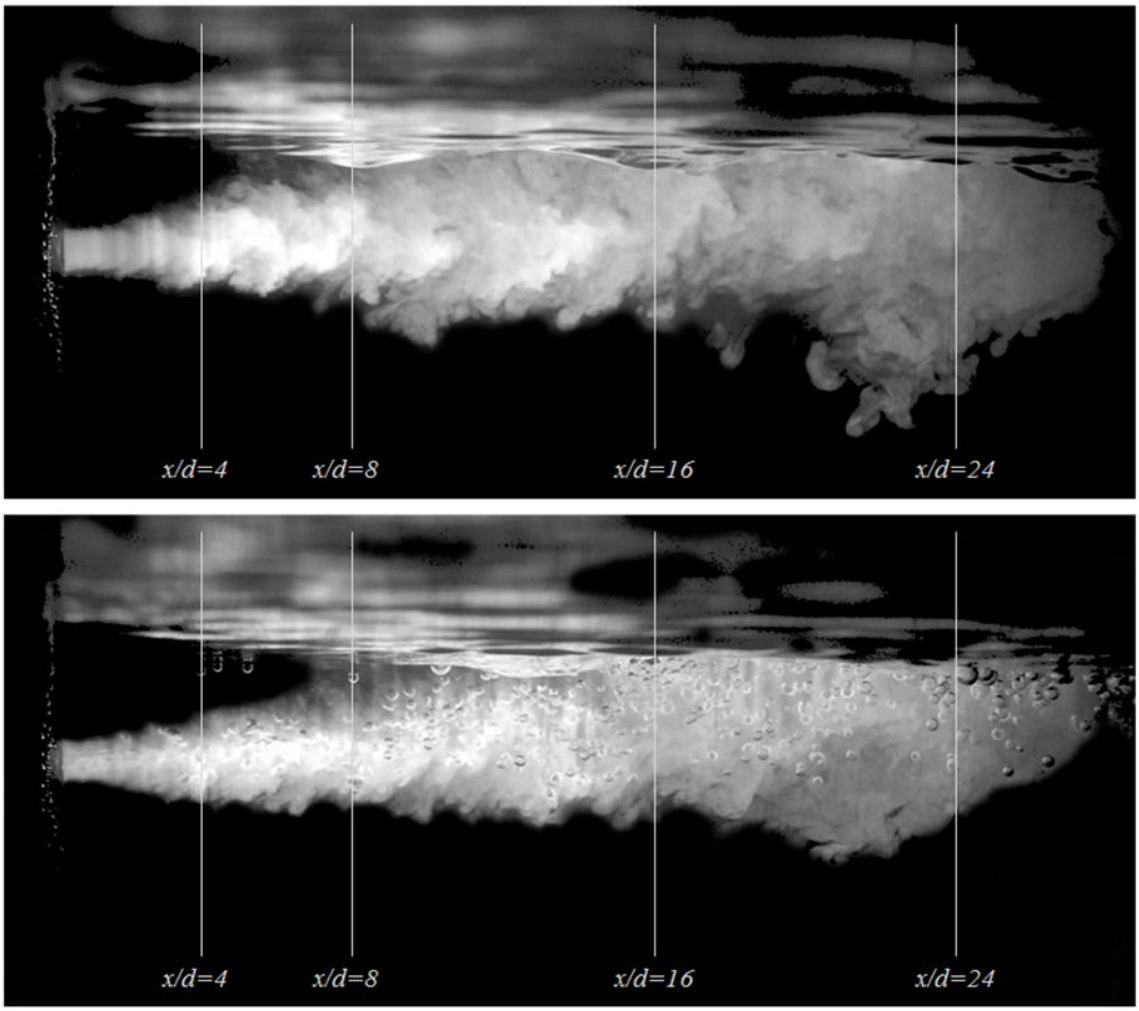

Figure 6: Short exposure view of the surface jet at $y/d = 0$. $Q_w = 3.41$ l/min and $Q_a = 0$ l/min (top), $Q_a = 0.4$ l/min (bottom).

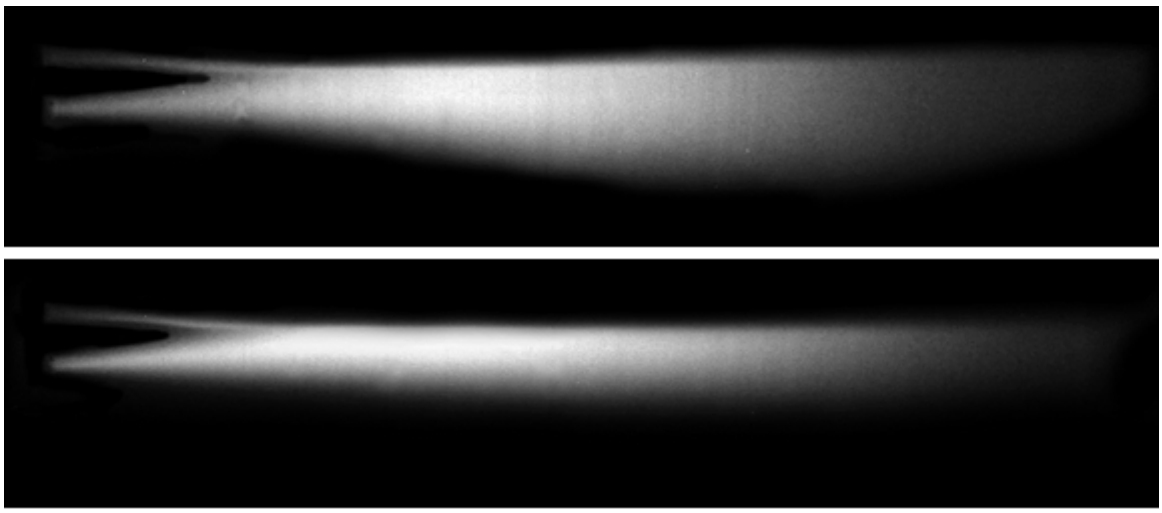

Figure 7: Long exposure view of the surface jet at $y/d = 0$. $Q_w = 3.41$ l/min and $Q_a = 0$ l/min (top), $Q_a = 0.4$ l/min (bottom)

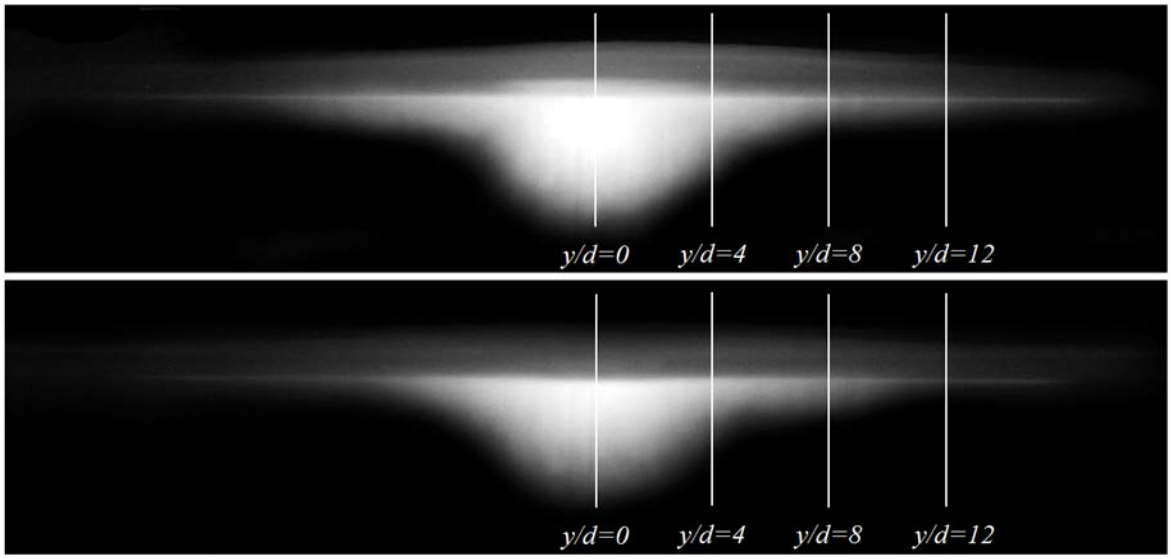

Figure 8: Long exposure view of the surface jet at $x/d = 32$. $Q_w = 3.41$ l/min and $Q_a = 0$ l/min (top), $Q_a = 0.4$ l/min (bottom).

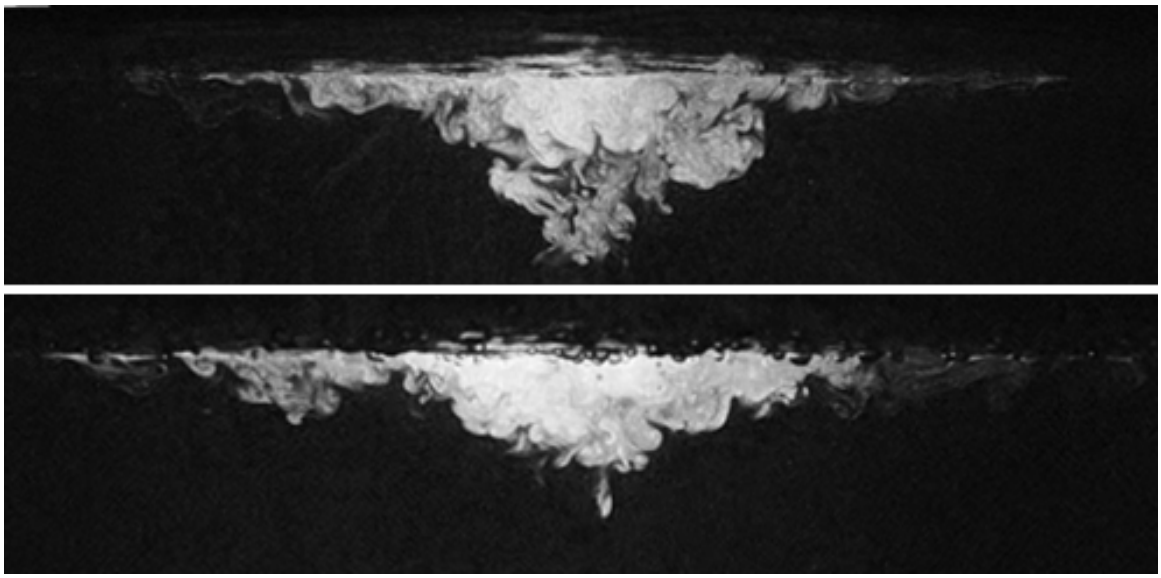

Figure 9: Short exposure view of the surface jet at $x/d = 32$. $Q_w = 3.41$ l/min and $Q_a = 0$ l/min (top), $Q_a = 0.4$ l/min (bottom).

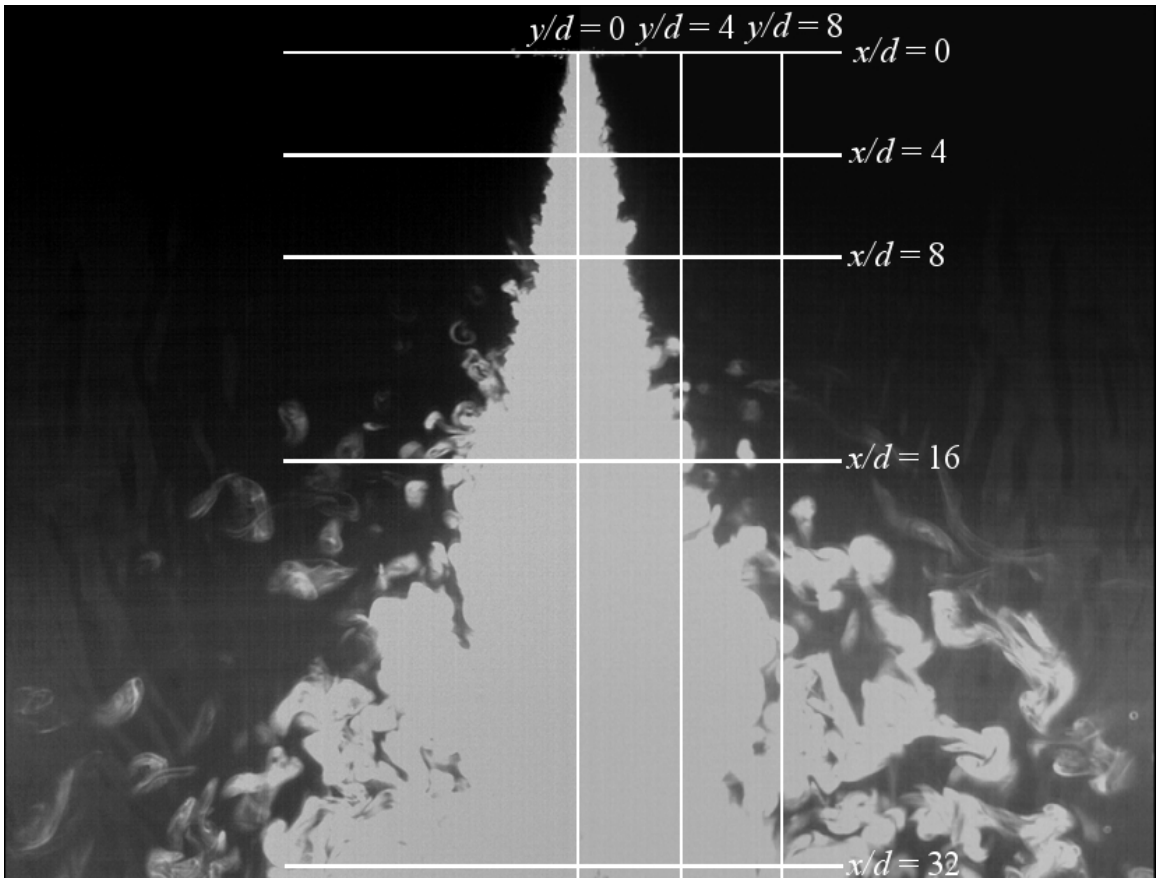

Figure 10: Instantaneous view of the surface jet from the top $Q_a = 0$ l/min (Left), $Q_a = 0.4$ l/min (Right).

3.2 Liquid measurements

3.2.1 Jet exit

The jet exit conditions were measured using stereo PIV as described in 2.3. Figure 11 and Figure 12 show the contours of axial mean velocity, axial velocity RMS fluctuations and turbulent kinetic energy very close to the jet exit (x/d~0.4), for $Q_w = 3.41$ l/min and $Q_a = 0$ and 0.4 l/min. The uncertainties in velocity were found to be 4.3% of $U_{0,w}$, mostly due to geometric errors and thus independent of the position, while corresponding uncertainty maps for RMS and TKE values, that contain a significant component of precision errors are shown.

Larger velocities are observed near the injection due to the increase in momentum when bubbles are injected. Without air injection, the presence of the injectors can be clearly seen as quasi-symmetric lobes in the axial velocity profile. In the two-phase jet, the axial velocity profiles are elongated in the vertical direction, likely due to non-uniform bubble injection. Axial velocity RMS fluctuations, which measures the intensity of the velocity fluctuations about the mean velocity, without air are in the order of 3~5%. These RMS values are relatively large, but still much smaller than fluctuations observed in the jet downstream. When air is injected at a rate of $Q_a = 0.4$ l/min, the RMS fluctuations of axial velocity increase approximately by a factor of 4, and become comparable with the RMS levels observed downstream in the jet. When bubbles are

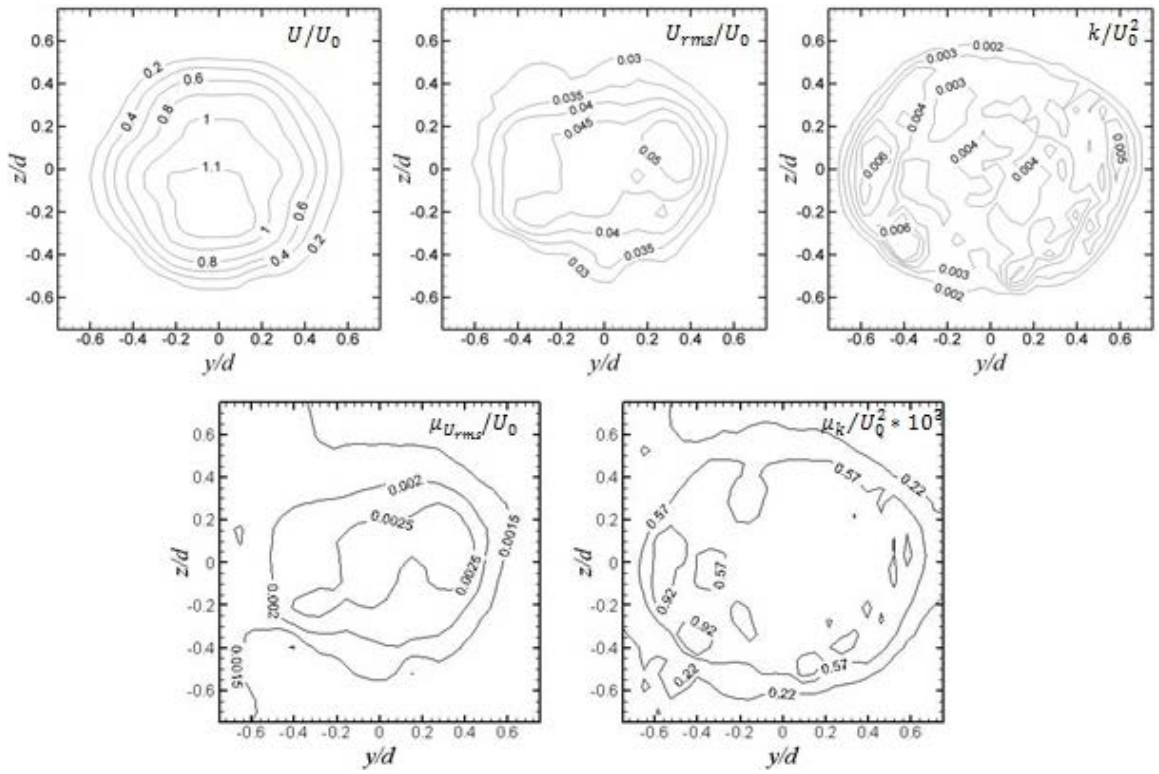

Figure 11: Jet exit conditions; $Q_w = 3.41$ l/min, $Q_a = 0$ l/min.

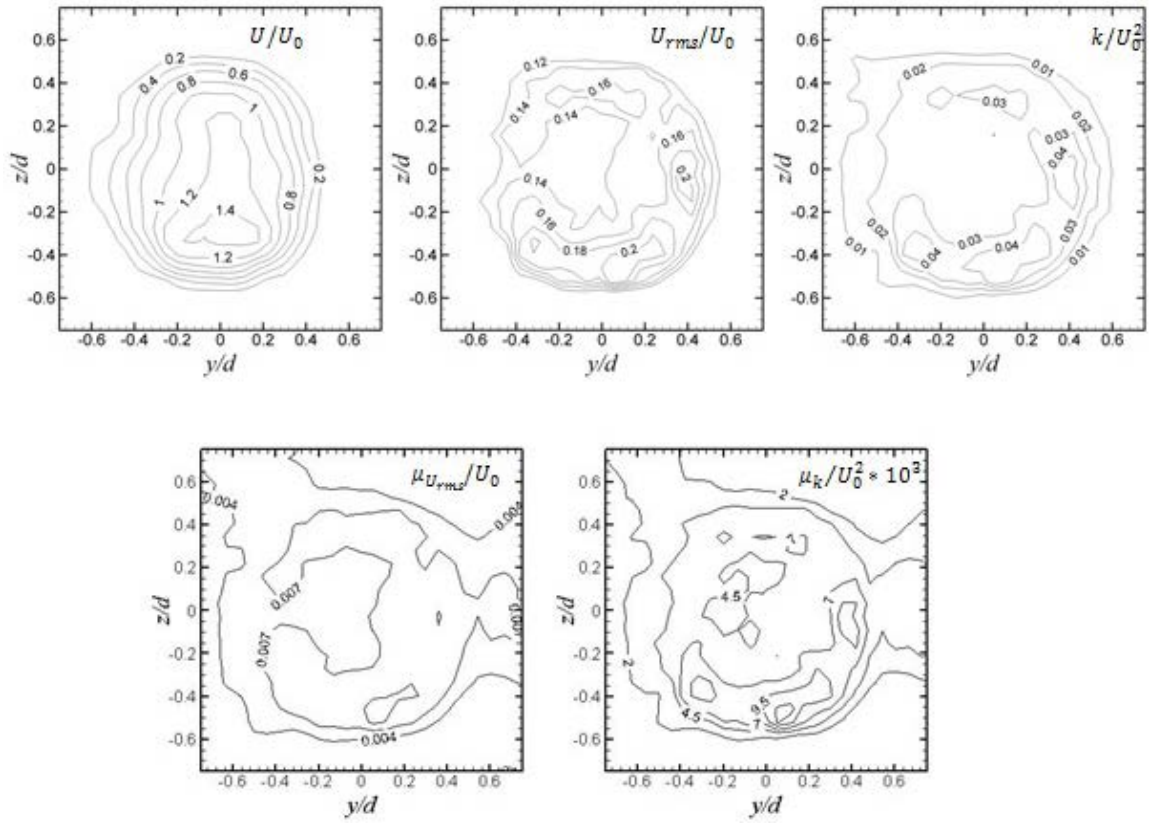

Figure 12: Jet exit conditions; $Q_w = 3.41$ l/min, $Q_a = 0.4$ l/min.

injected, the turbulent kinetic energy increases one order of magnitude with respect to the case with no air injection. This is due to the bubbles, which present an obstacle that needs to be accelerated to the liquid velocity as they detach from the injectors. The unsteady nature of the injection, as bubbles detach periodically, provides a mechanism to produce velocity fluctuations and turbulence. The presence of the injectors can be seen where highs in RMS fluctuations and turbulent kinetic energy are measured. Note also that the uncertainty in RMS is approximately 6%, slightly higher for the two-phase than for the single-phase measurements, while the uncertainty in kinetic energy is higher than 10%.

3.2.2 Jet core velocities and Reynolds stresses

Liquid velocities in the axial and vertical directions in the core of the jet were measured using 2D LDV. Vertical traverses at the centerline $y = 0$ and horizontal traverses near the free surface at $z/d = 1.6$ were evaluated at several constant x/d axial positions as described in 2.8.

Axial and vertical velocities and Reynolds stresses (non-dimentionalized by$U_{0,w}$, 2.8) in vertical and horizontal planes are shown in Figure 13 and Figure 14, respectively. The measured values without air injection compare qualitatively well with those by Walker *et al*. [8], but the results fit better their high Reynolds number jet than their smallest jet that is closest with the conditions in this work ($Re = 12700$, $Fr = 8.0$ for Walker *et al*. [8], $Re = 13080$, $Fr = 7.21$ for this work). The difference between Walker's and our results is probably caused by the more turbulent nature of our jet due to the air injection needles, which then behaves more as a higher Reynolds number jet.

Figure 13 shows vertical and horizontal profiles of axial and vertical liquid velocities at different axial positions along the flume. Notice that the uncertainties for the axial velocity are typically 1~3% and are within the size of the symbols, with larger errors when large gas volume fractions are involved (lower data rate with bubbles) and in the core of the jet where more fluctuations are present. For the vertical velocity the absolute uncertainties are of magnitude similar to those for the axial velocities, thus having much larger relative errors. Similar observations can be made for the Reynolds stress measurements, which carry larger precision errors. The location of the free surface at rest is at $z/d = 2$. At $x/d = 8$, the axial velocities for the single- and two-phase jets are very similar, but the two-phase jet is located slightly higher. The immediate consequence is that the bubbly jet is higher than the single phase jet at all stations, as shown in the axial velocity profiles in Figure 13. The distance between the jet core and the free surface decreases when bubbles are injected, increasing the axial velocity near the free surface. At $x/d \geq 16$, the maximum liquid velocity when gas is injected is

24.7% higher than that measured for the single phase jet. Consistent with a higher jet, the axial velocities of the jet at depth are smaller when bubbles are injected. The velocity difference due to bubble injection is more pronounced at depth and increases with the streamwise distance. At $x/d = 32$, the velocity of the single phase jet at depth is still significant, whereas in the case when bubbles are injected undisturbed water is found due to the faster attraction of the two-phase jet towards the free surface, indicating that, while the jet is attracted to the free surface faster in the two-phase case, no significant diffusion is added in the process. The minimum vertical downward velocity increases with the distance from the injector. A clear increased upward velocity is observed when bubbles are present, causing the jet to move higher and attach to the free surface faster than the single-phase jet. While single-phase surface jet attraction to the free surface has been observed by other researchers [4, 5, 8], an immediate effect of bubbles is to drag liquid upward as the bubbles rise. According to Figure 13, the vertical velocity increases at all axial stations when air is injected, with a maximum between $x/d = 16$ and 24, where the vertical velocity reaches about 35 mm/s higher than in the single phase case. Note that the estimated vertical relative velocity between bubbles and water for the bubble sizes measured in this experiment is approximately 250 mm/s. At $x/d = 32$ the core of the jet has reached the free surface and few bubbles remain, resulting in very small vertical velocity. Note that the vertical velocity is not zero near the free surface, mostly for $x/d = 8$, though it decreases approaching it for all axial positions and it could be small or zero at the free surface where LDV measurements were not possible. However, jet-induced surface waves exhibit a strong positive slope at $x/d = 8$, and thus any axial velocity translates into a vertical velocity component. The free surface elevation results are discussed in section 3.2.6.

Figure 13 also shows that the lateral spread of the jet increases considerably with respect to the single-phase jet as the jet attaches to the free surface, for higher x/d positions. As the jet attaches to the free surface, the core of the jet extends sideways,

increasing the lateral reach of the core. This would be consistent with the presence of stronger surface currents, first reported by Anthony and Willmarth [5] for single phase flows, when bubbles are present. The presence of strong surface currents is reinforced by the concentration of high vertical velocity on the centerplane observed mostly at $x/d = 8$ and 16. This high vertical velocity can only be consistent with mass conservation if a lateral velocity is developed, since the axial velocity decreases downstream of the jet.

Vertical and horizontal profiles of the Reynolds stresses are shown in Figure 14. The normal axial Reynolds stress is stronger for the two-phase jet, but the normal vertical Reynolds stresses are damped compared to the single-phase jet. In both cases the vertical stresses are damped near the free surface, though free surface fluctuations prevent the normal vertical Reynolds stresses from going to zero at the free surface. Downstream, and as the two-phase jet is attracted to the free surface faster, the axial Reynolds stresses are slightly higher near the free surface for the two-phase jet but considerably lower deeper in the flow. This is consistent with a higher jet when bubbles are injected, which reduces axial velocity and turbulence at depth. Overall, the normal Reynolds stresses are damped by the presence of bubbles in the bulk of the liquid, but very close to the free surface the effect is reversed and the Reynolds stresses increase slightly when bubbles are present. This is likely due to the larger free surface elevation fluctuations observed with bubbles, see section 3.2.6. Part of these free surface fluctuations are irrotational, caused by traveling waves or bubbles leaving the free surface, and thus not due to turbulence. This phenomenon, in the context of free surface waves, has been discussed by Voulgaris and Trowbridge [36], who propose a method based on using spatial correlations to identify surface fluctuations and remove them from the Reynolds stresses. The method, designed for large-scale experiments, would be very difficult to apply in the scale of the present research. Since bubbles increase considerably the velocity fluctuations tangential to the free surface, more anisotropy is observed in the two-phase jet near the free surface.

The Reynolds shear stress $< u'w' >$ is negative at deeper locations, as turbulent eddies shed downward and carry high axial momentum deeper into the flow. The same trend, with positive $< u'w' >$, is observed for $x/d \leq 16$ for positive z close to the free surface and before the jet core reaches to it, the same phenomenon indicating high axial velocity eddies mixing with higher, lower velocity flow. This behavior is also seen in the y traverse at $z/d = 1.6$ in Figure 14, where the cross correlation is positive for $x/d \leq 16$ and negative (but small) farther from the jet exit. Indeed, the shear Reynolds stress magnitude increases slightly when bubbles are present very near the free surface ($z/d = 1.6$) and off the centerplane. As opposed to the normal stresses, $< u'w' >$ is less positive farther out from the free surface with the presence of bubbles ($0 < z/d < 1.6$) and less negative as well for deeper locations ($-5 < z/d < 0$). This clearly indicates that the net turbulent viscosity decreases when large bubbles are introduced, the same trend observed in other flows like turbulent boundary layers [37] and vertical channels [38], where turbulence attenuation has also been reported.

Notice in Figure 14 that for $x/d > 16$ the axial Reynolds stress $< u'u' >$ peaks away from the vertical centerplane, at $y/x \sim 0.05$, and then drops rapidly as the distance to the centerplane increases. This area of larger axial fluctuations is accompanied by a quick decrease in axial velocity (see Figure 13), but does not exhibit any remarkable change in $< u'w' >$ and $< w'w' >$. This indicates the boundary of the jet near the free surface, where fluctuations in the vertical velocity are constrained by the free surface fluctuations and should have little correlation with the axial velocity.

Measurements with $Q_w = 3.41$ l/min and $Q_a = 0.4$ l/min were carried out at different depths, from $z/d = -0.4$ to $z/d = 1.6$ in intervals of $z/d = 0.4$, and for $x/d = 16$ and 32. Plots of average axial and vertical velocity and Reynolds stresses are shown in Figure 15. The axial velocity shows that at $x/d = 16$, U peaks below the free surface, see also Figure 13. However, at $y/d = 3$ the maximum velocity occurs closest to the free surface, again indicating the presence of bubbles strengthens the surface currents

reported by Anthony and Willmarth [5] which carry high axial momentum fluid away from the centerplane and along the free surface (see section 3.2.5). At $x/d = 32$ the jet has spread considerably, and is mostly attached to the free surface and the axial velocity peaks at the free surface for all lateral positions. The vertical velocity shows a peak at $x/d = 16$, $z/d = -0.4$ near $y/d = 0.2$, which coincides with the boundary of the jet core, and then stabilizes inside the jet core. At $x/d = 32$, the vertical velocity is smaller and decreases significantly near the free surface except closer to the centerplane. The vertical velocity peaks approximately at $y/d = 0.45$ as the fringes of the jet core rise to fully attach to the free surface.

Outside the jet core ($y/d > 0.2$) the Reynolds stresses decrease rapidly, and inside the axial normal Reynolds stress is over twice as large as the vertical Reynolds stress, showing a significant anisotropy. Notice that at $x/d = 16$ the free surface is about $\zeta = 0.7d$ above the level at rest (Figure 21), and thus the highest position of the probe is still about 1.1 d below the water. The vertical velocity peaks at $z/d = 0.8$ inside the core of the jet, and though it decreases further up, it is still too far from the free surface to vanish.

At $x/d = 16$ the shear Reynolds stress $< u'w' >$ exhibits negative values at deeper locations inside and through the boundary of the jet core, and turns positive above $z/d = 1.2$, indicating that the jet core is still accelerating liquid above it and thus has not completely attached to the free surface. At $x/d = 32$ $< u'w' >$ remains negative at all depths. The vertical normal Reynolds stress $< w'w' >$ closest to the free surface and inside the jet core implies RMS fluctuations of the vertical velocity of about $W_{rms}/U_0 = \sqrt{< w'w' >}/U_0 = 0.038$, similar values observed for the free surface elevation fluctuations shown in Figure 21. This suggests that a very significant portion of these RMS fluctuations are due to free surface oscillations and not necessarily due to turbulence.

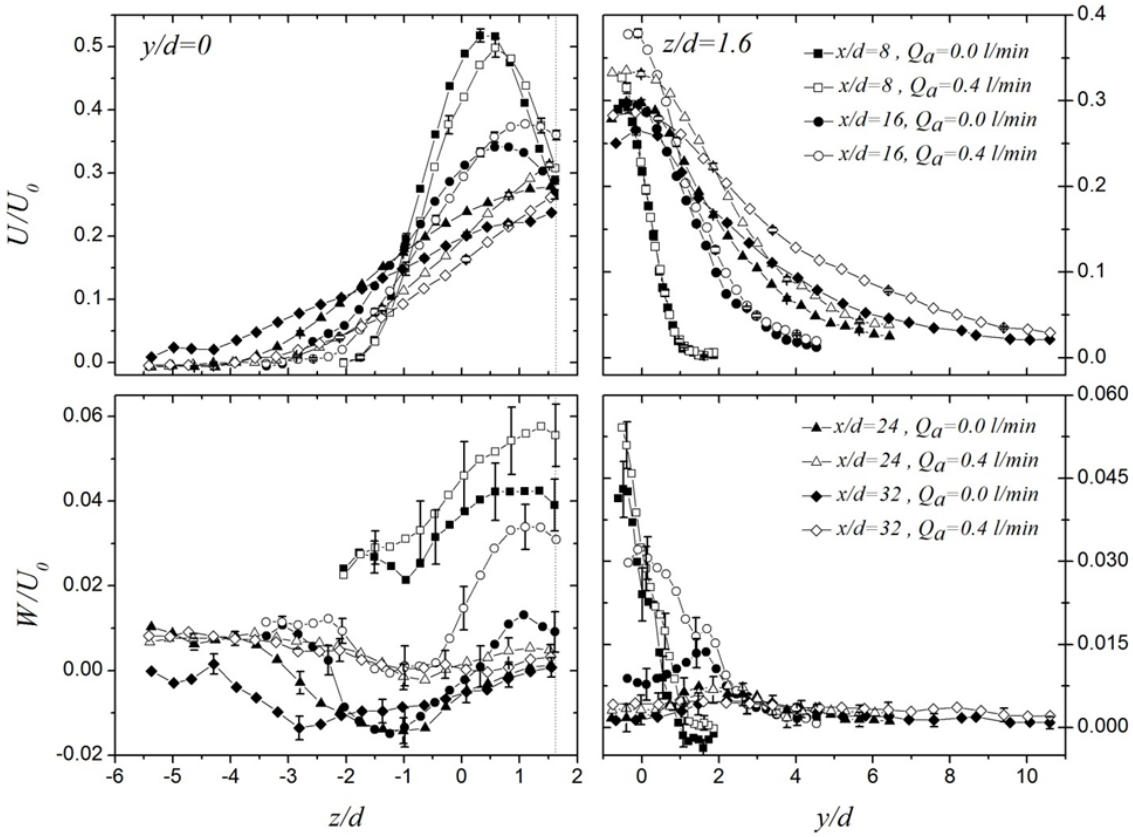

Figure 13: Liquid axial (top) and vertical (bottom) velocities for vertical (left) and horizontal (right) traverses at different axial positions for $Q_w = 3.41$ l/min and $Q_a = 0$ and 0.4 l/min.

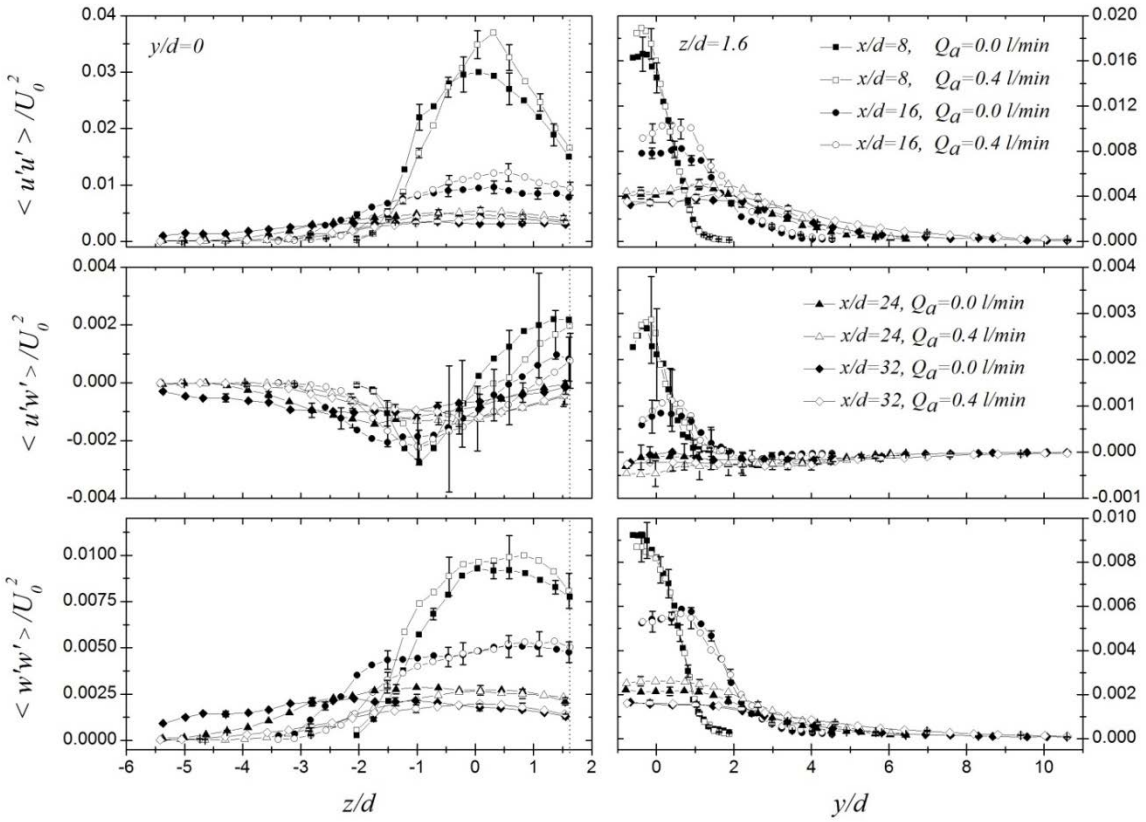

Figure 14: Reynolds stresses for vertical (left) and horizontal (right) traverses at different axial positions for $Q_w = 3.41$ l/min and $Q_a = 0$ and 0.4 l/min. $u'u'$ (top), $u'w'$ (center) and $w'w'$ (bottom).

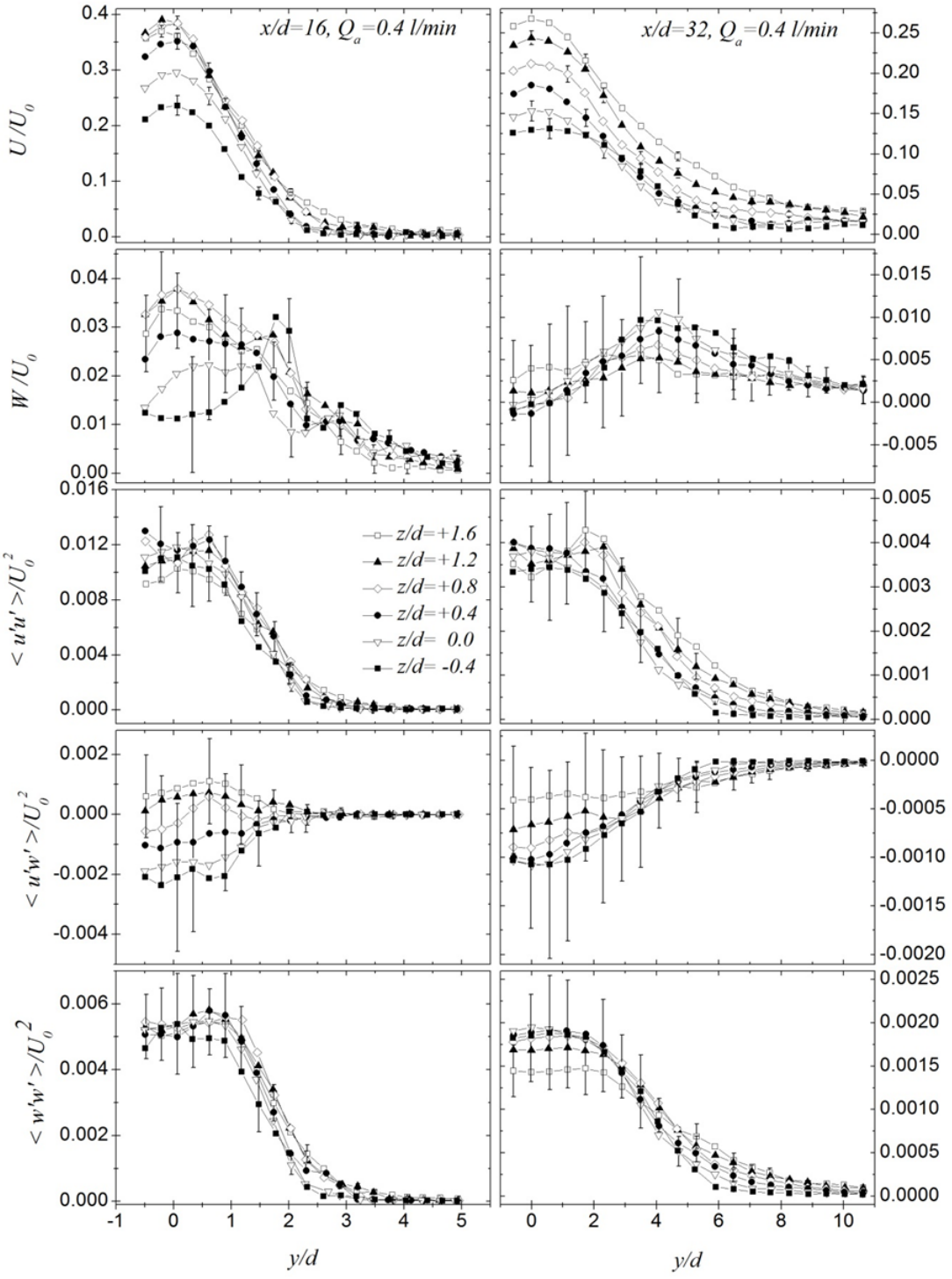

Figure 15: Average velocity and Reynolds stresses at different depths for $Q_w =$ 3.41 l/min and $Q_a =$ 0.4 l/min at $x/d = 16$ and 32.

3.2.3 Jet far field

The far field flow was measured using stereo PIV with a domain size of size $18d \times 18d$ encompassing both positive and negative y locations.The velocity and kinetic energy fields for $Q_w = 3.41$ l/min, $Q_a = 0$ l/min and $Q_a = 0.4$ l/min at planes $x/d = 8$ and $x/d = 16$ are shown in Figure 16. As discussed in section 2.3, these measurements are limited by the dynamic range of the PIV system. An approximate location of the boundary of confidence can be inferred where the axial velocity has the maximum, as marked in Figure 16. Figure 16 shows that the bubbly jet is closer to the free surface (located at approximately $z/d = 2$) when bubbles are present. The surface currents (see 1.2), are clearly observed in Figure 16 for $x/d = 16$ but not present yet at $x/d = 8$, was. The attraction to the free surface when bubbles are present results also in much more limited reach of the vortices issuing below the jet core, evidenced by the turbulent kinetic energy shown in Fig. 5. Notice also that the presence of surface currents transport fluid from the jet core, creating a high axial momentum layer near the free surface that was not present at $x/d = 8$.

3.2.4 Water entrainment

The far field flow was measured using stereo PIV in a domain size of size $18d \times 18d$ encompassing positive and negative y locations. The velocity and kinetic energy fields for $Q_w = 3.41$ l/min, $Q_a = 0$ l/min and $Q_a = 0.4$ l/min at planes $x/d = 8$ and $x/d = 16$ are shown in Figure 16. As discussed in section 2.3, these measurements are limited by the dynamic range of the PIV system, and hence, an approximate location of the boundary of confidence can be inferred where the axial velocity has the maximum, as marked in Figure 16. The surface currents (see 1.2), are clearly observed in Figure 16 and are discussed further in section 3.2.5.

As a free jet loses momentum, it accelerates surrounding fluid, resulting in entrainment of fluid to the jet. The axial volumetric flow rate Q of the jet and surrounding fluid is given by [13]:

$$Q = \int_0^{2\pi} \int_0^{\infty} U(r,\theta) r dr d\theta \quad (6)$$

Mass conservation relates the change in axial volumetric flow rate with the radial velocity as

$$dQ/dx = \int_0^{2\pi} u_r r d\theta \quad (7)$$

where u_r is the radial velocity towards the jet and r is a radial coordinate from the axis of the jet exit that is used to define the surface to compute Q. Ideally, as r increases dQ/dx should converge, though this convergence may be slow and take many jet diameters to happen, see for instance [22]. The entrainment rate can be computed as an instantaneous quantity, or as the time average, as reported in this work, by using converged average velocities to compute u_r. Notice that in Equation (7) the air volume fraction effect is not considered since no bubbles are present far from the jet axis.

In the case of a surface jet the integral in Equation (7) cannot be computed for all angles due to the presence of the free surface, but integration within the water phase is still valid. The accuracy of the computation of the integral in Equation (7) decreases as the radius increases, due to increased uncertainty of the PIV computations as the velocity decreases. Notice also that near the free surface the presence of surface currents (see section 3.2.5) create a local negative entrainment, which has to be accounted for to compute the entrainment.

Several mechanisms compete to increase or decrease the entrainment in a bubbly jet with respect to a single-phase jet. The presence of bubbles reduces the effective viscosity, an effect that reduces entrainment while entrainment is increased as bubbles leave the jet through the free surface and their volume is replaced by liquid, causing entrainment to fill the void. It is not clear how bubbles will modify the processes of nibbling and engulfment, where non-turbulent fluid in engulfed into the turbulent core and converted into turbulent motion, nibbling [39].

The resulting asymptotic entrainment rate is presented in Figure 17. It is observed that the entrainment clearly decreases with higher air flow rate. It peaks at $x/d = 8$ for the case with no air injection and then decreases farther away from the jet exit. For $Q_a = 0.2$ l/min the peak in entrainment is barely distinguishable and occurs at $x/d \sim 12$, and for $Q_a = 0.4$ l/min the entrainment increases monotonically with increasing distance from the jet exit with a somewhat asymptotic trend. The behavior of the entrainment rate for $Q_a = 0$ l/min is similar to that observed by Liepmann and Gharib [6] for a larger diameter jet (25.4 mm) at lower Reynolds number ($Re = 6000$). The presence of a peak in the entrainment is explained by Liepmann and Gharib [6] by an initial development similar to that of a submerged jet, but as the jet approaches the free surface the entrainment from the top is restricted and the asymptotic entrainment rate is about half of that of a free jet. As discussed in 3.2, the presence of bubbles increases the upward flow, but mass conservation will result in an outward flow near the free surface, thus removing any significant effect on entrainment. On the other hand, the overall reduction of the turbulence observed on the fringe of the jet would produce less mixing and then resulting in less entrainment.

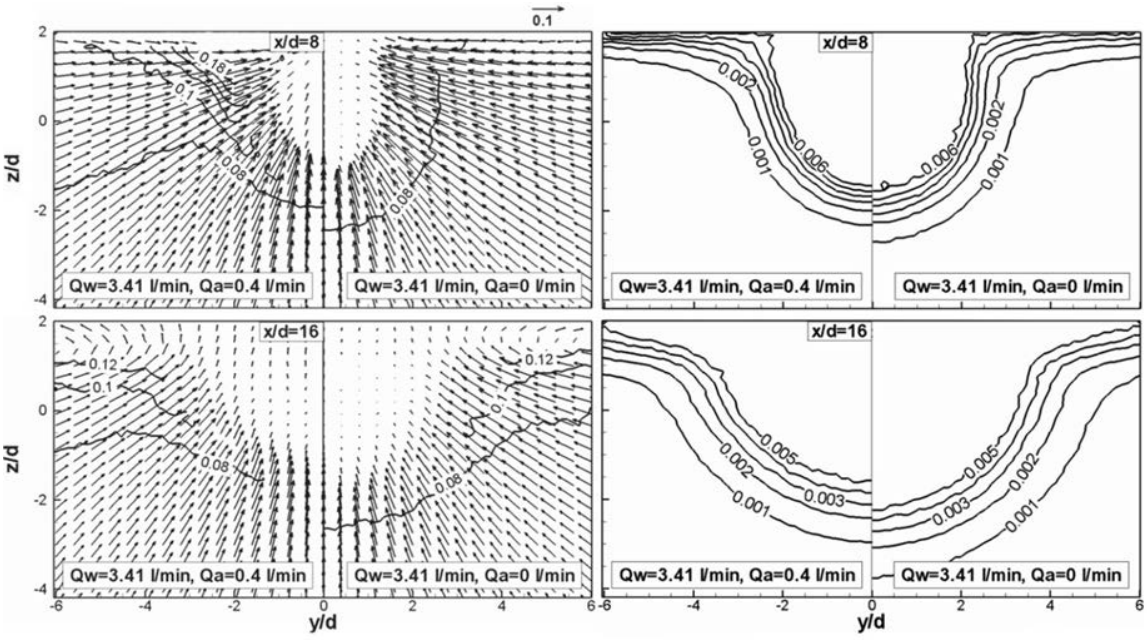

Figure 16: Axial and transversal velocity vectors (U/U_0, left) and turbulent kinetic energy (k/U_0^2, right) for $x/d = 8$ (top) and $x/d = 16$ (bottom).

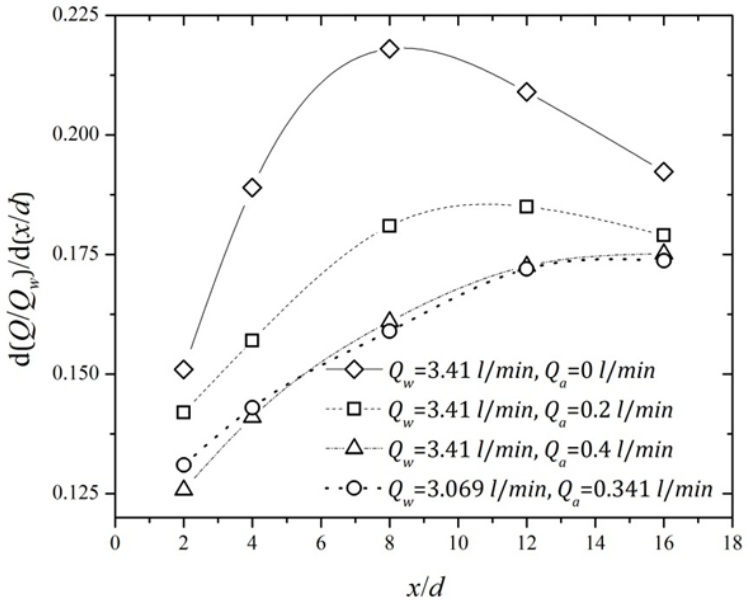

Figure 17: Asymptotic entrainment rate at different longitudinal locations.

3.2.5 Surface currents

The use of the surface PIV technique (2.4) permits measurements of mean velocities on the free surface, removing through averaging the elliptical velocity caused by the waves. While changes on the free surface location greatly affect PIV and LDV measurements, which are fixed in space and thus do not follow fluctuations on the position of the interface, surface PIV uses positively buoyant particles to maintain the measurements at the free surface.

Figure 18 shows the dimensionless velocity at the free surface for $Q_a = 0$ l/min and 0.4 l/min, while Figure 19 and Figure 20 show the axial and lateral velocities and corresponding RMS values at specific measurement planes. The strength of the surface current can be measured in terms of the lateral velocity U_y/U_0. As expected, the lateral velocity approaches zero at the far field and at the symmetry plane, resulting in a peak in the surface current that occurs approximately at $y/x \cong 0.2$. For $x/d > 16$, the strength of the surface currents is significantly higher when air is injected in the jet, increasing 25% at the peak at $x/d = 24$ and over 60% at $x/d = 32$. At $x/d = 8$, before the jet core reaches the free surface, the surface current is weak. At $x/d = 16$ the surface current strength is already considerable but similar for the cases with and without bubbles.

The axial velocity in Figure 19 follows the same trend as the lateral velocity, though the changes observed when bubbles are present are much more moderate. It is worth noticing that these lateral velocities are taken into account when computing the entrainment (causing a local negative entrainment), resulting in smaller entrainment when the surface currents are stronger. This effect can partially explain the decrease in entrainment observed when bubbles are injected (Figure 16).

The RMS of the velocity, shown in Figure 20, is greatly affected by the waves that add a wave-induced motion measured by the particles. The differences between the RMS of the velocity with or without air injection become important at higher distances

from the injector. The magnitude of the fluctuations is considerable, reaching 65% of the lateral velocity at the peak and 15% of the axial velocity at the center plane.

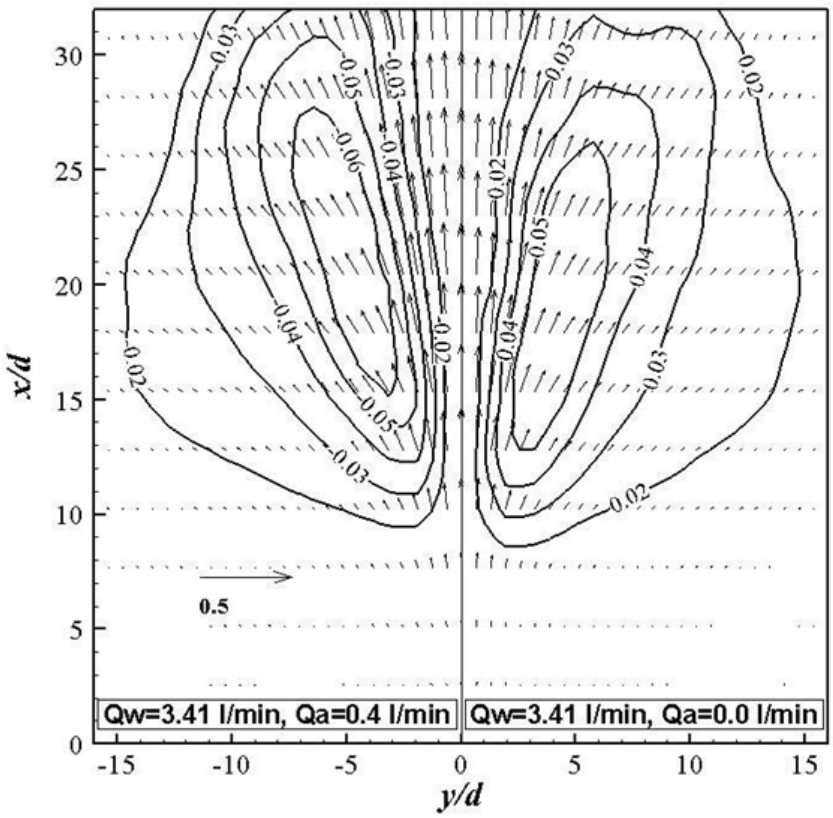

Figure 18: Mean dimensionless free surface velocity vectors (U_x/U_0, U_y/U_0) and transversal velocity contours for $Q_a = 0$ l/min (right) and $Q_a = 0.4$ l/min (left).

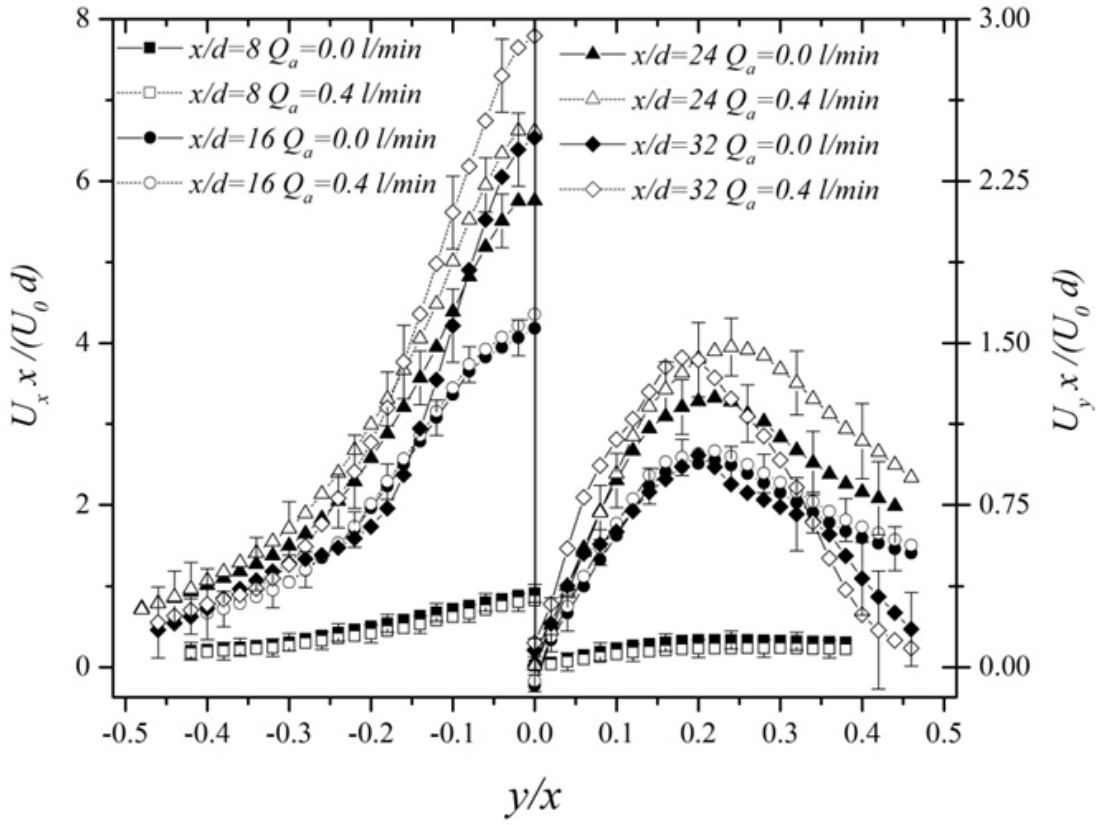

Figure 19: Average axial (left) and traversal (right) velocity profiles at different axial positions for $Q_w = 3.41$ l/min with $Q_a = 0.0$ l/min and $Q_a = 0.4$ l/min.

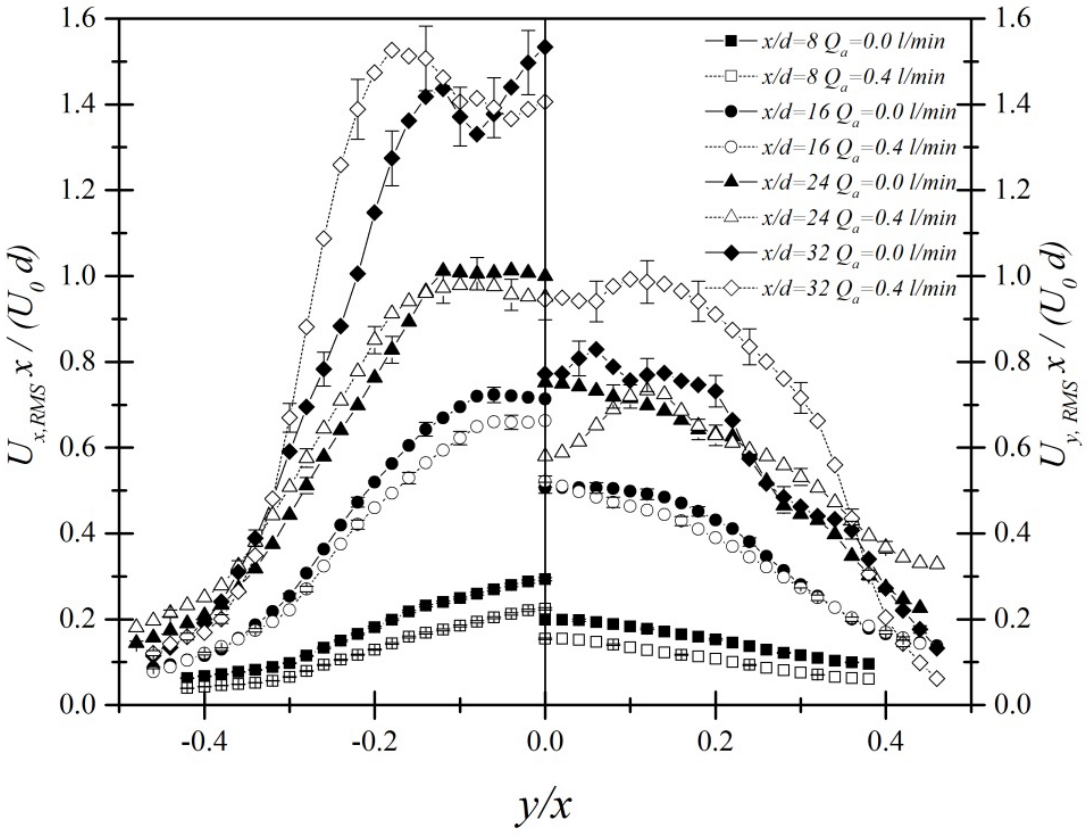

Figure 20: RMS of Average axial (left) and traversal (right) velocity profiles at different axial positions for for $Q_w = 3.41$ l/min with $Q_a = 0.0$ l/min and $Q_a = 0.4$ l/min.

3.2.6 Free surface elevation

The free surface elevation was measured using a novel technique developed for this project. The idea is to slowly lower a phase detection probe (at a rate of 5 cm/hr) and compute the air volume fraction according to Eq. (2), using a small integration time of 30 s. The air volume fraction as a function of depth is then obtained. From this the mean free surface elevation and the RMS fluctuations can be obtained as:

$$\zeta_{av} = \frac{1}{1-\alpha_{min}} \int_{\alpha_{min}}^{1} z d\alpha \qquad (8)$$

$$\zeta_{rms} = \sqrt{\frac{1}{1-\alpha_{min}} \int_{\alpha_{min}}^{1} (\zeta_{av} - z)^2 d\alpha} \qquad (9)$$

where α_{min} is the minimum air volume fraction measured in the water side caused by the presence of bubbles.

Figure 21 shows the mean free surface elevations and the free surface RMS fluctuations measured along the $y = 0$ and $x/d = 16$ lines, for the cases with $Q_w = 3.41$ l/min and $Q_a = 0$ and 0.4 l/min. The jet creates a free surface wave with a wavelength that is mostly unaffected by bubbles. After an initial suction of the free surface caused by the jet exit, the mean elevation peaks at $x/d = 12$ for the cases with no air injection and with $Q_a = 0.4$ l/min, and then reaches a trough at approximately $x/d = 24$. Bubbles change considerably the amplitude of the wave. The increase in the jet axial momentum when bubbles are injected results in a larger initial free surface deflection. At $x/d = 8$ and $y/d = 0$, the free surface elevation with and without bubbles is the same. At $x/d = 16$, the mean free surface elevation peaks at the centerplane and the maximum depression is observed at $y/d = 4$. At $y/d = 0$ and for $8 < x/d < 20$ and at $x/d = 16$ and for $0 < y/d < 2$ the free surface is higher when bubbles are injected. This region coincides with higher upward velocity of the jet due to the bubbles (Figure 13). The maximum mean surface elevation increases by 30% when air is injected.

The RMS fluctuations peak also at $x/d = 12$ for the case with no air injection, so the mean free surface elevation and the RMS fluctuations both peak together for the baseline case. Conversely, for $Q_a = 0.4$ l/min the RMS fluctuations peak around $x/d = 20$, where the mean free surface elevation is moving to a trough. The RMS fluctuations decay with the distance from the jet core, and exhibit higher amplitude with air injection than without air. The larger RMS fluctuations of the free surface with air are possibly due to the increased fluctuations caused by the bubbles leaving the free surface. Error estimations were not attempted for the free surface elevation measurements.

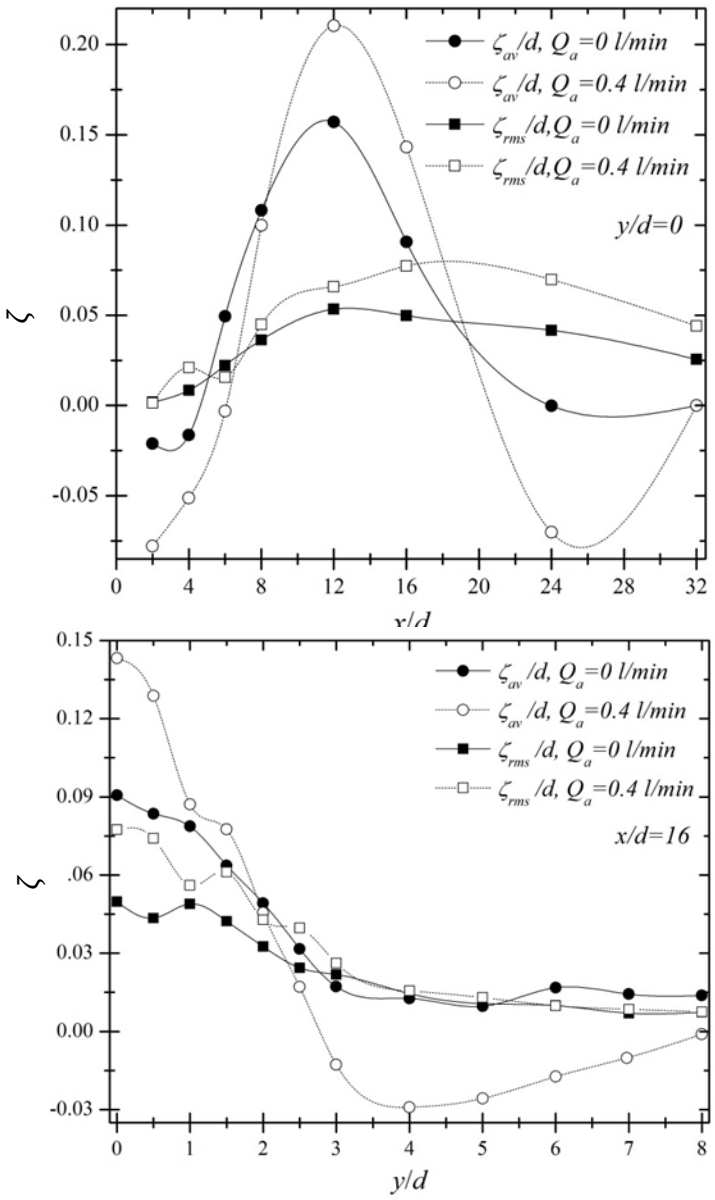

Figure 21: Mean free surface elevation and RMS for several axial positions x/d and at the centerplane $y = 0$ (top) and at $x/d = 16$ for several lateral positions (bottom).

3.2.7 Effect of the presence of bubbles

LDV measurements near the free surface at the center plane of the jet $y = 0$, $z/d = 1.6$, were taken for $Q_w = 3.41$ l/min and Q_a from 0 l/min to 0.4 l/min in intervals of 0.05 l/min. Figure 22 shows axial and vertical average velocities and the RMS of their

fluctuations for $x/d = 8, 16, 24$ and 32. The effect on the axial velocity is small and in line with the increase expected caused by the net higher volume flow rate (see 2.8). The axial velocity RMS fluctuations also change little, mostly at $x/d = 32$ when the bubbles almost completely left the flow and are essentially not present in the axis of the jet. The effect on the vertical velocity, however, is more important. At $x/d = 16$ the effect on the vertical velocity is maximum, and increases over 200% at the highest air flow rate studied (Case 1) with respect to the baseline case with no air injection (Case 0). Then the vertical velocity decreases as the distance to the jet exit increases but the volumetric rate of air injection still has a significant effect on the vertical velocity. The RMS fluctuations of the vertical velocity show, as in the case of the axial velocity, a small increase with increasing air flow rate, with the exception of the measurements at $x/d = 8$. At this location, the vertical normal Reynolds stresses are relatively small and insensitive to the air injection flow rate, see Figure 15.

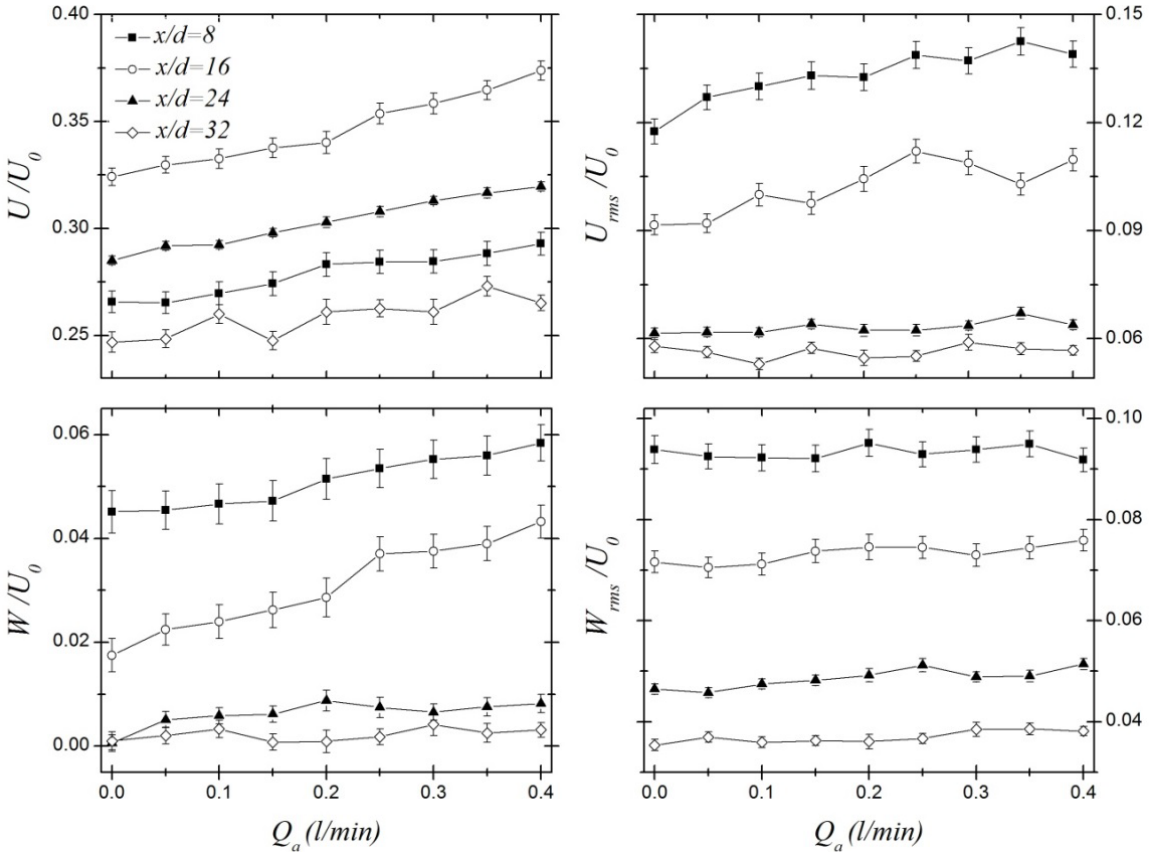

Figure 22: Axial velocity (top-left) and RMS (top-right) and vertical velocity (bottom-left) and RMS (bottom-right) for $Q_w = 3.41$ l/min and variable Q_a at $x/d = 8, 16, 24$ and 32, $y = 0$, $z/d = 1.6$.

3.3 Two-phase flow quantities

3.3.1 Air volume fraction

Figure 23 shows the average air volume fraction (Eq. 2) as a function of depth and lateral position at the vertical center plane $y = 0$ and the horizontal plane $z = 0$. Measurements were carried out under the three conditions shown in Table 1, $Q_w = 3.41$ l/min with $Q_a = 0.2$ and 0.4 l/min, and $Q_w = 3.069$ l/min with $Q_a = 0.341$ l/min, and at two axial position positions $x/d = 8$ and 16. It is clear from Figure 23 that at $x/d = 8$ the bubbles have risen more in the case with the lowest liquid velocity $Q_w = 3.069$ l/min due to a higher vertical to axial bubble velocity ratio. At $x/d = 16$ the bubbles have

mostly risen almost to the free surface, showing a peak there. In both cases the bubbles are higher than the jet core, see Figure 13 for comparison. Since the bubbles rise quickly, the air volume fraction drops accordingly at higher depths, and at $z = 0$ the air volume fraction is very small for $x/d = 16$ at all transversal positions.

Figure 24 shows the air volume fraction at the vertical center plane $z = 0$ with $Q_w = 3.41$ l/min with $Q_a = 0.4$ l/min at seven axial positions from $x/d = 2$ to $x/d = 32$. The peak air volume fraction decreases rapidly from about 13% at $x/d = 2$ to about 5% at $x/d = 12$, while the bubbles rise and disperse. Notice a considerable accumulation, already observed in Figure 23 at $x/d = 16$, of bubbles near the free surface for $x/d = 12$ and higher, peaking at $x/d = 24$. This is due to the decrease in rising velocity as the bubbles approach the free surface, and the time needed to dry the liquid film and coalesce with the free surface to finally allow the air to exit the flow. The time it takes a 1 mm air bubble in ethanol to coalesce with the free surface is approximately 50 ms, being longer for bigger bubbles in water [40].

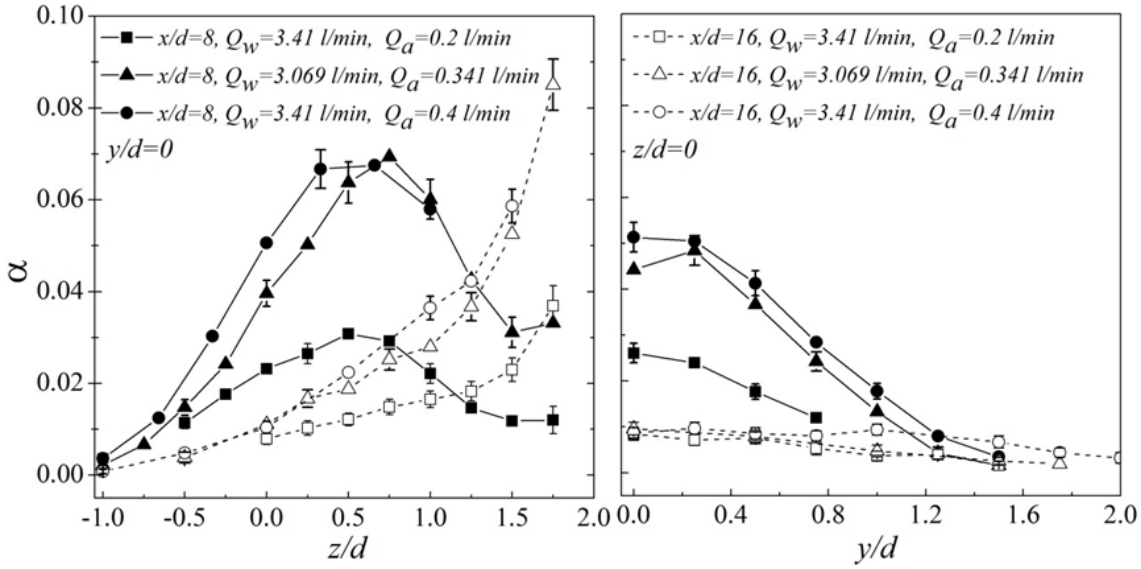

Figure 23: Air volume fraction for vertical (left) and horizontal (right) traverses at different volumetric flow rates of water and air. The free surface is located at $z/d = 2$.

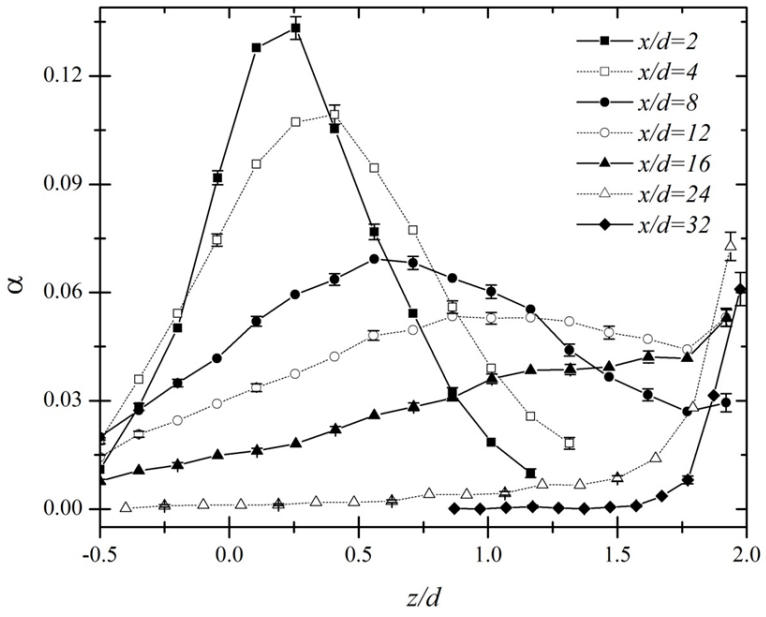

Figure 24: Air volume fraction at different axial positions on the centerplane for $Q_w =$ 3.41 l/min and $Q_a =$ 0.4 l/min. The free surface is located at $z/d = 2$.

3.3.2 Bubble chord length

The average chord length (Equation 3), shown in Figure 25, exhibits interesting features. At $x/d = 2$, the average chord length at deeper locations tends to be larger. This is probably caused by the bubble rising velocity opposing dispersion velocity below the injection axis and causing extra bubble collision and coalescence. Above the injection axis, buoyancy and dispersion move in the same direction, reducing coalescence. This effect is also visible, but to a much less extent, at $x/d = 4$ and $x/d = 8$. Coalescence along the axial direction is also evident as the chord length increases with axial position. The chord length also increases dramatically near the free surface, where longer contact time between bubbles strongly favors coalescence. Close visual examination (Figure 27) of the jet shows significant bubble coalescence near the free surface. In Figure 27, a single bubble is tracked as it coalesces three times along the free surface prior to breaking through the free surface In addition to this effect, natural filtering occurs due to the higher rising velocity of larger bubbles, resulting in larger bubbles at higher positions as the smaller bubbles take longer to rise. At $x/d = 32$ the two effects are evident, with much smaller bubbles at deeper locations than near the surface. Notice also that the error in the average chord length quickly rises as fewer bubbles are counted farther away from the jet exit. This is due to the large variation in chord length measured as bubbles are pierced along shorter or longer chords for similarly sized bubbles, thus needing significantly more statistics to converge than the air volume fraction [33].

3.3.3 Bubble velocity

The mean time-of-flight bubble velocity (Equation 2) is shown in Figure 26. Though the optical phase detection probes can measure the velocity directly, the uncertainty is relatively large since there is a considerable indetermination on the active region of the probe tip [33]. To reduce the uncertainty, the probe velocity measurements were calibrated against the velocity obtained from high-speed video taken at 1400 f/s at

the center plane and $x/d = 8$ by measuring time of flight of individual bubbles across a reference line in each frame of the high speed video. Still Figure 26 reports the uncertainty before calibration, with the calibration points shown with cross symbols. As the axial distance to the jet exit increases and the jet spreads and rises, the bubbles follow the same trend as they are mainly transported by the liquid in the axial direction. The bubble axial velocity near the free surface is lower than in the bulk of the flow for all axial positions, as opposed to the liquid axial velocity that peaks at the free surface far from the jet exit, see Figure 13 and Figure 15. At $x/d = 32$ the bubble velocity peaks at approximately $z/d = 1.6$ (still consistent with the liquid velocity in Figure 15), and then drops 15% when it reaches the free surface.

Before reaching the free surface (at approximately $x/d = 16$), the bubble velocity above the jet core drops rapidly. This is caused by bubbles leaving the high axial momentum jet core due to gravity. As the bubbles leave the jet core they drag some high-momentum liquid with them from the jet core (the virtual mass), but bubbles slow down quickly essentially to the local axial fluid velocity. Periodically, turbulent eddies carry some high axial velocity bubbles to this region of the flow, resulting in some degree of smoothing on the velocity profile above the jet.

Another interesting feature in Figure 26 is that the bubble velocities decay much more slowly than the liquid velocities below the jet. As turbulent eddies reach outside the core of the jet (see the negative Reynolds shear stress $< u'w' >$ in Figure 14 below the jet), they carry high axial velocity bubbles that are detected and measured by the probe. At these same locations there are no bubbles when there are no eddies transporting them from the core of the jet, and that time the axial bubble velocity would be low. Therefore, since the bubble velocity is conditional to having bubbles and the bubbles originate from the jet core, they have much higher average velocity outside the jet core than the liquid does.

Normalized bubble velocity distributions at four axial locations and different vertical locations at the center plane are shown in Figure 28. The bubble velocities close to the jet ($x/d = 2$) and near the jet axis are around 1.5 m/s, with fluctuations of over 10%, consistent with the PIV measurements at the jet exit (see Figure 11 and Figure 12). At higher locations, farther from the jet axis, the velocity decreases and velocities can become negative. This pattern is repeated downstream, with the additional characteristic that the distributions become narrower and the velocities more uniform, this last behavior already seen in Figure 26.

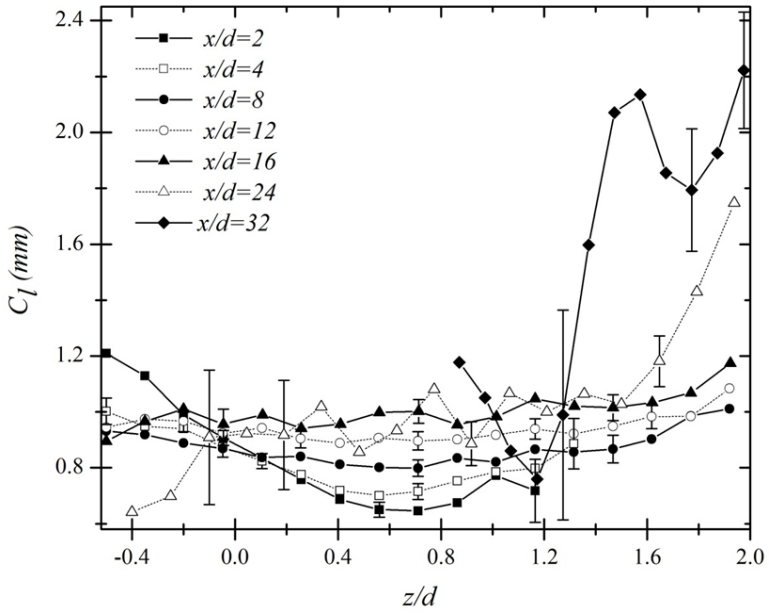

Figure 25: Average bubble chord length at different axial positions on the centerplane for $Q_w = 3.41$ l/min and $Q_a = 0.4$ l/min. The free surface is located at $z/d = 2$.

3.3.4 Bubble size distributions

The bubble size distribution along the axis of the jet ($y = z = 0$), computed as described in Johansen *et al*. [33], is shown in Figure 29. The methodology followed assumes that the bubbles are spherical, from photographic observation this is a good

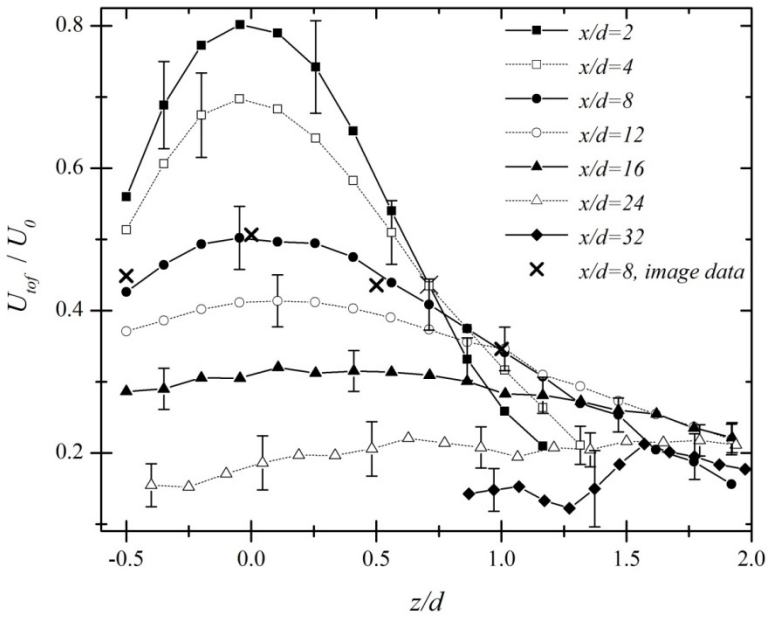

Figure 26: Bubble velocity at different axial positions on the centerplane for $Q_w = 3.41$ l/min and $Q_a = 0.4$ l/min. The free surface is located at $z/d = 2$.

assumption away from the jet exit (see Figure 6). In Figure 29, the bubble size probability density function $f(d, \mathbf{x}, t)$ and the size probability $P(d, \mathbf{x}\, t)$ are related by:

$$f(d, \mathbf{x}, t) = N(\mathbf{x}, t)P(d, \mathbf{x}, t) \quad (10)$$

where $N(\mathbf{x}, t)$ is the bubble number density, related to $f(d, \mathbf{x}, t)$ by:

$$N(\mathbf{x}, t) = \int_0^\infty f(d, \mathbf{x}, t)dd \quad (11)$$

Notice that Equations (10) and (11) imply that the integral of $P(d, \mathbf{x}\, t)$ is 1. As the jet expands and the air volume fraction decreases away from the jet axis, there is initially a decrease in bubble size (from $x/d = 2$ to $x/d = 4$) and then a gradual increase. The increase in average size as the distance to the jet increases is evident in Figure 29. The shift in the size distribution toward smaller bubbles from $x/d = 2$ to $x/d = 4$ is due to the bubbles turning spherical from the initial prolate spheroidal shape

aligned to the jet axis generated by the air injector as the bubbles detach. This shape results in longer chord lengths for the same bubble volume, showing up in the size probability as bigger bubbles. Indeed, Figure 29 shows clear evidence of coalescence as the bubbles are transported downstream of the jet exit. The main collision mechanisms are a) turbulent fluctuations and b) velocity gradients occurring as the jet spreads and the velocity decreases, bringing the bubbles closer to each other. Coalescence then occurs if the bubbles remain in contact long enough to break up the film of liquid separating them [41]. An example of bubble coalescence in the bulk of the flow can be seen in Figure 30.

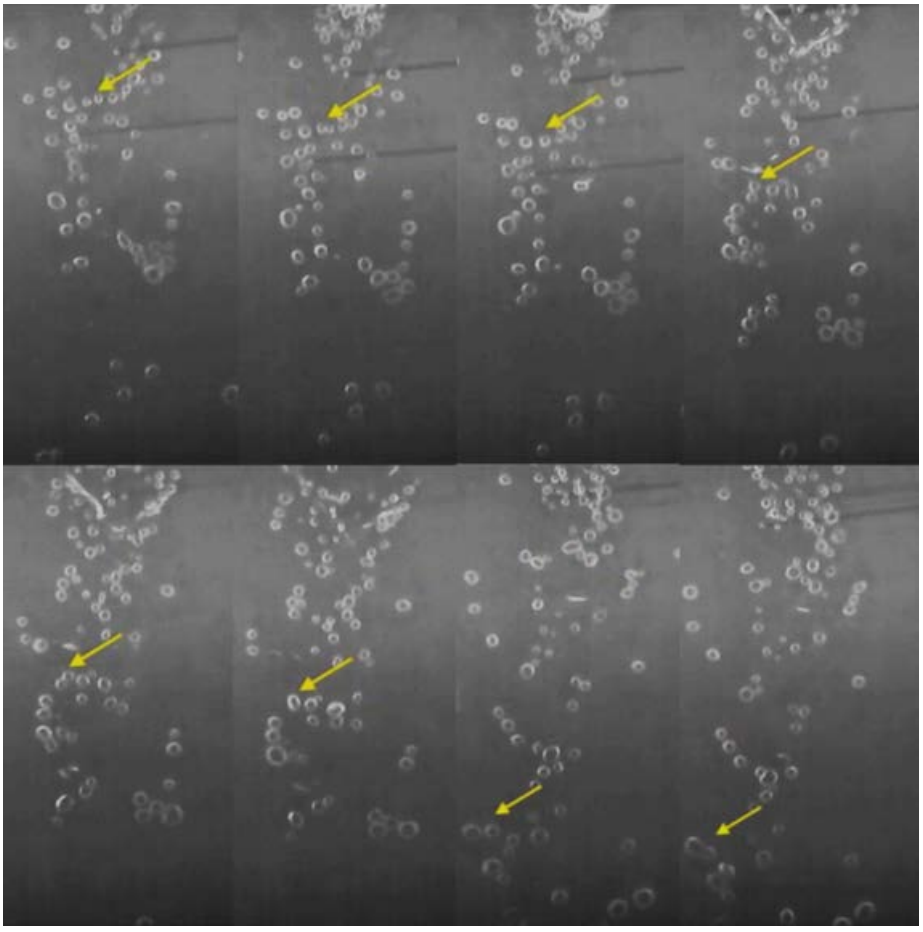

Figure 27: Surface bubble coalescence starting at approximately $x/d = 24$.

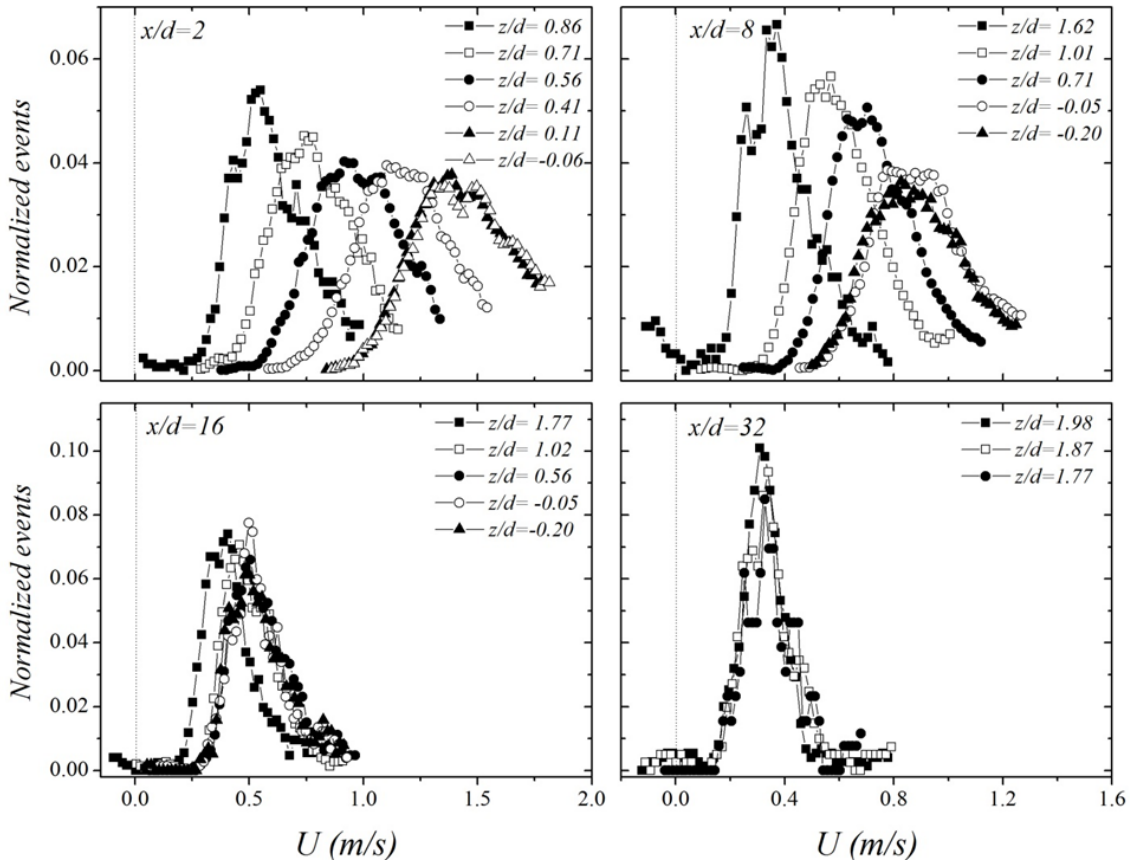

Figure 28: Velocity distributions at different axial positions on the centerplane.

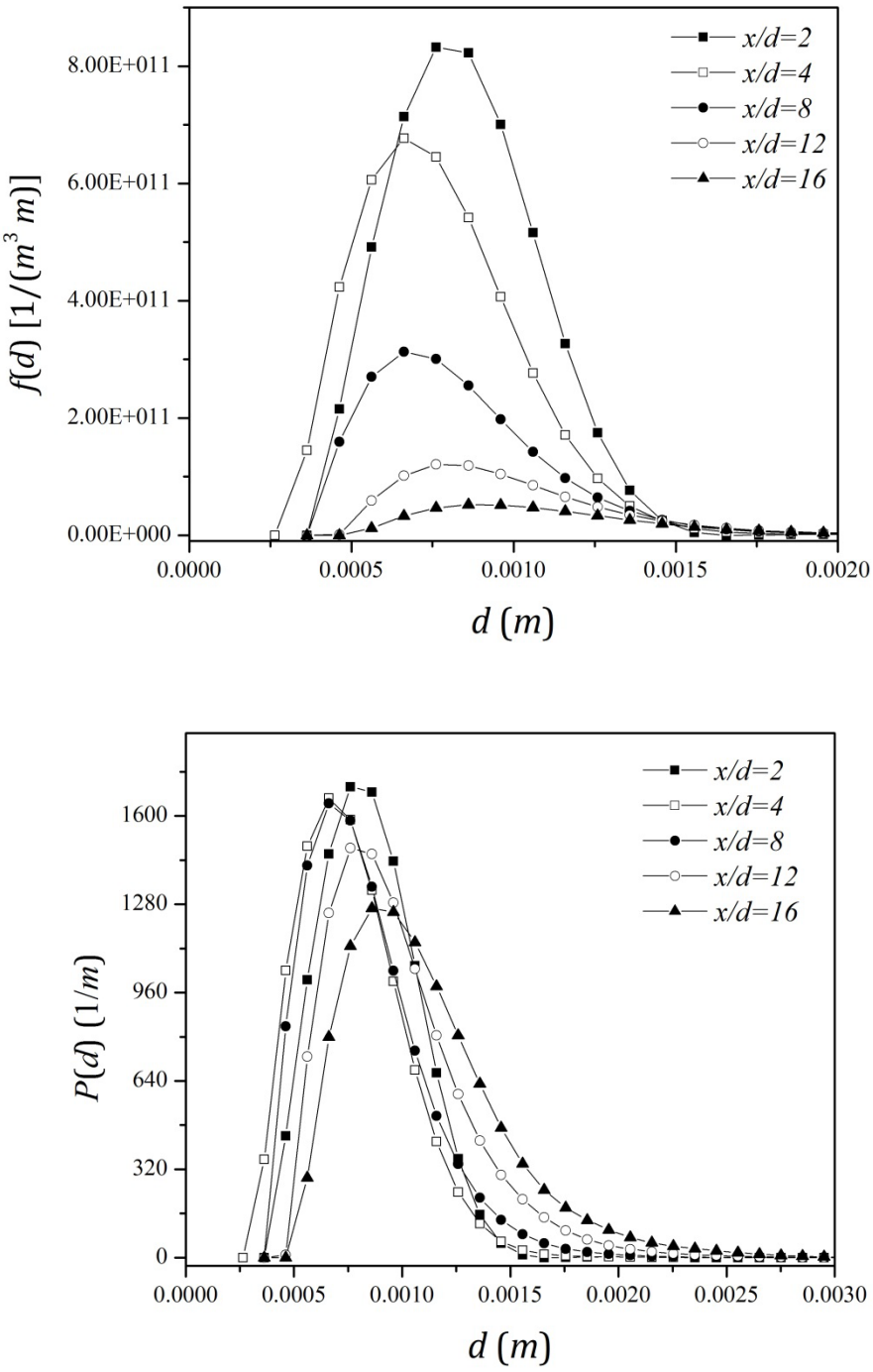

Figure 29: Bubble size probability density function (top) and size probability $P(d) = f/N$ (bottom) for $Q_w = 3.41$ l/min and $Q_a = 0.4$ l/min.

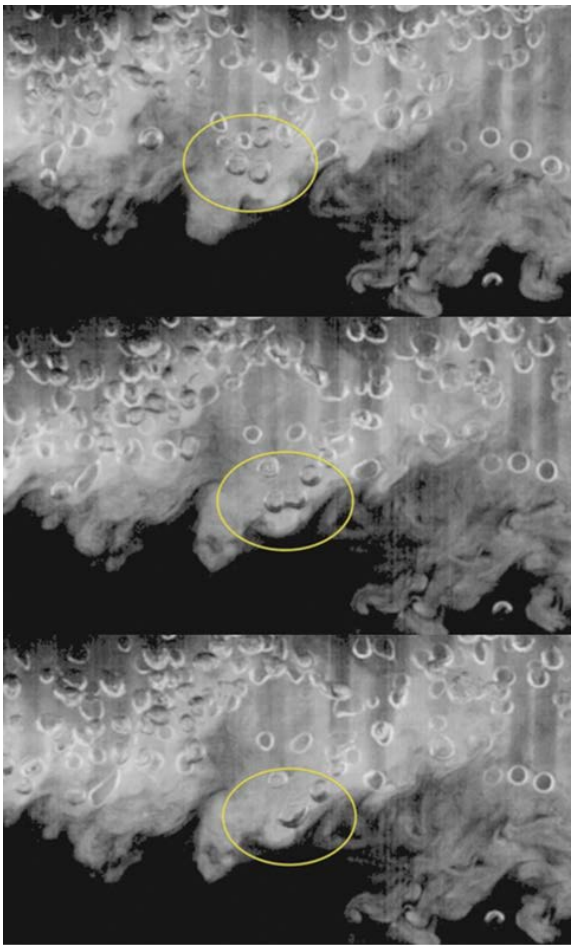

Figure 30: Bubble coalescence in bulk of flow along centerplane for $Q_w = 3.41$ l/min and $Q_a = 0.4$ l/min, approximate location $x/d = 8, z/d = -0.5$.

CHAPTER 4: CONCLUSION

This experimental study was motivated to advance the understanding of two-phase surface jets. Results show that the presence of bubbles drag the liquid of the jet upward as they rise which causes the jet to reach and attach to the free surface earlier and consequently produce more lateral spread near the interface than the single-phase jet.

The momentum transfer from the bubbles to the liquid is also evident on the increased vertical velocities measured at all locations when bubbles are present. It is interesting to note that the axial velocities, though reflect that the jet moved higher with the presence of bubbles, increased only slightly, mostly near the free surface. The normal Reynolds stresses are damped by the presence of bubbles in the bulk of the liquid, but very close to the free surface the effect is reversed and the normal stresses increase slightly when bubbles are present. The Reynolds shear stress $< u'w' >$ is negative at deeper locations, as turbulent eddies shed downward carry high axial momentum deeper into the flow. The same trend, with positive $< u'w' >$, is observed for positive z close to the free surface and for $x/d \leq 16$, before the jet core reaches the interface. The presence of bubbles causes a decrease in Reynolds shear stress at all locations except very near the free surface, indicating that the bubbles are attenuating the turbulence.

The effect of bubbles on the entrainment shows a clear decrease in entrainment with higher air flow rates: for the same water flow rate, as the air flow rate increases from $Q_a = 0.0$ l/min to 0.4 l/min, the maximum rate of entrainment decreases up to approximately 22%. Conversely though, the lateral velocity, used to quantify the strength of the surface current, increases with the injection of bubbles. Near the jet exit, before the jet core reaches the free surface, the surface current is weak, but becomes significant for $x/d \geq 16$. By injecting bubbles, the strength of the surface currents increases significantly at higher distance from the injector, up to over 60% at $x/d = 32$.

The results of the two-phase variables show interesting trends. The air volume fraction shows that the bubbles rise quickly and the peak on volume fraction moves to the interface approximately at $x/d = 16$. The accumulation of bubbles near the free surface is evident, resulting in higher air volume fraction and coalescence rate that results in larger bubbles farther away from the jet exit. Natural filtering due to the slower rising velocity of smaller bubbles is also observed. Strong coalescence is observed as the jet develops, with the average chord length increasing over 20% from $x/d = 8$ to $x/d = 16$ for all cases studied. The bubble velocities are more uniform than the liquid velocities, since bubbles are carried to the boundaries of the jet by liquid vortices with high axial momentum, resulting in higher velocities than the local liquid velocities.

REFERENCES

[1] Weitkamp DE, Katz M, A review of dissolved-gas supersaturation literatura. *Trans. Am. Fish. Soc.* 109:659–670, 1980.

[2] Politano MS, Carrica PM, Turan C, Weber L, A multidimensional two-phase flow model for the total dissolved gas downstream of spillways. *J. Hydr. Res.* 45(2): 165-177, 2007

[3] Turan C, Politano M, Carrica PM, Weber L, A study of the water entrainment on Wanapum Dam. *32nd IAHR Congress*, Venice, Italy, 2007

[4] Liepmann D, The near-field dynamics and entrainment field of submerged and near surface jets. Ph.D. thesis, University of California, San Diego, 1990.

[5] Anthony DG, Willmarth WW, Turbulence measurements in a round jet beneath a free surface. *J. Fluid Mech.* 243:699-720, 1992.

[6] Liepmann D, Gharib M, The vorticity and entrainment dynamics of near-surface jets. In *Free-Surface Turbulence* (ed. E. P. Kood and J. Katz). ASME FED-181, p. 53, 1994.

[7] Madnia CK, Bernal LP, Interaction of turbulent round jet with the free-surface. *J. Fluid Mech*. 261:305-332, 1994.

[8] Walker DT, Chen CY, Willmarth WW, Turbulence structure in free-surface jet flows. *J. Fluid Mech*. 291:223-261, 1995.

[9] Trujillo MF, Hsiao C, Choi J, Paterson EG, Chahine GL, Peltier LJ, Numerical and experimental study of a horizontal jet below a free surface. *9th Int. Conf. Numerical Ship Hydrodyn*., Ann Arbor, MI, 2007.

[10] Walker DT, Chen CY, Evaluation of algebraic stress modeling in free-surface jet flows. In *Free Surface Turbulence* (ed. E. P. Rood and J. Katz). ASME FED-181, p.83, 1994.

[11] Turan C, Politano M, Carrica PM, Weber L, Water entrainment due to spillway surface jets. *Int. J. Comp. Fluid Dyn*. 21:137-153, 2007.

[12] Walker DT, On the origin of the ‘surface current’ in turbulent free-surface flows. *J. Fluid Mech*. 339:275-285, 1997.

[13] Wygnanski I, Fiedler H, Some measurements in the self-preserving jet. *J. Fluid Mech*. 38:577-612, 1969.

[14] Murzyn F, Mouaze D, Chaplin JR, Flow visualization and free surface length scales measurements in a horizontal jet beneath a free surface. *Exp. Thermal Fluid Sci*. 30: 703-710, 2006.

[15] Newman BG, The deflexion of plane jet by adjacent boundaries. Coanda effect in *Boundary layer and flow control*, Ed. G. V. Lachman, Pergamon Press, Oxford, 1961.

[16] Launder BE, Rodi W, The turbulent wall jet-measurements and modeling. *Ann. Rev. Fluid Mech*. 15:429-459, 1983.

[17] Walker DT, Johnston VG, Observations of turbulence near the free surface in the wake of a model ship. In Dynamics of bubbles and vortices near a free surface, *ASME AMD*-119, (Ed. I. Sahin and G. Tryggvason), 1991.

[18] Hoekstra M, Macro wake features of a range of ships. MARIN Rep. 410461-1-P. Maritime Research Institute Netherlands, 1991.

[19] Morton BR, Taylor GI, Turner JS, Turbulent gravitational convection from maintained and Instantaneous sources. *Proc. R. Soc. London*, Ser. A 235, 1–23, 1956.

[20] Townsend AA, *The structure of turbulent shear flow*. Cambridge University Press, 1976.

[21] Baddour RE, Zaghloul A, Martunizzi R, Entrainment properties of plane surface jets in shallow current. *J. Hyd. Eng*. 132:363-370, 2006.

[22] Liepmann D, Gharib M, The role of streamwise vorticity in the near-field entrainment of round jets. *J. Fluid Mech*. 245:643-768, 1992.

[23] Sun TY, Faeth GM, Structure of turbulent bubbly jets. 1. Methods and centerline properties. *Int. J. Multiphase Flow* 12:99–114, 1986.

[24] Lima Neto IE, Zhu DZ, Rajaratnam N, Bubbly jets in stagnant water. Int. *J. Multiphase Flow* 34:130-1141, 2008.

[25] Akhmetbekov Y, Alekseenko S, Dulin V, Markovich D, Pervunin K, Planar fluorescence for round bubble imaging and its application for the study of an axisymmetric two-phase jet. *Exp. Fluids* 48:615–629, 2010.

[26] Lima Neto IE, Zhu DZ, Rajaratnam N, Horizontal injection of gas–liquid mixtures in a water tank. *J. Hyd. Eng*. 134:1722-1731, 2008.

[27] Pedocchi F, Martin JE, Garcia MH, Inexpensive fluorescent particles for large-scale experiments using particle image velocimetry. *Exp. Fluids* 45:183–186, 2008.

[28] ITTC, Uncertainty Analysis Particle Imaging Velocimetry. *ITTC Procedure* 7.5-01-03-03, 2008.

[29] Lee SL, Durst F, On the motion of particles in turbulent duct flow. Int. J. Multiphase Flow 8:125-146. *Int. J. Multiphase Flow* 8, 125-146, 1982.

[30] Mudde RF, Groen JS, Van Den Akker HEA, Application of LDA to bubbly flows. *Nuc. Eng. Des.* 184:329-338, 1998.

[31] ITTC, Uncertainty Analysis: Laser Doppler Velocimetry Calibration. *ITTC Procedure* 7.5-01-03-02, 2008.

[32] Cartellier A, Achard JL, Local phase detection probes in fluid/fluid two-phase flows. *Rev. Sci. Instrum*. 62:279-303, 1991.

[33] Johansen JP, Castro AM, Carrica PM, Full-scale two-phase flow measurements on Athena research vessel. *Int. J. Multiphase Flow* 36:720-737, 2010.

[34] Carrica PM, Sanz D, Zanette D, Delgadino G, Di Marco P, A Contribution to the Uncertainties Estimation in Local Void Fraction Measurements in Gas-Liquid Flows. *Int. Symp. Two-Phase Modeling Experim.*, Rome, Italy, 1995.

[35] Wallis GB, *One-dimensional two-phase flow*. Mc-Graw Hill, 1967.

[36] Voulgaris B, Trowbridge JH, Evaluation of the Acoustic Doppler Velocimeter (ADV) for turbulence measurements. *J. Atmos. Oceanic Tech*. 15: 272–289, 1998.

[37] Lu J, Fernandez A, Tryggvason G, The effect of bubbles on the wall drag in a turbulent channel flow. *Phys. Fluids* 17:095102, 2005.

[38] Hosokawa S, Tomiyama A, Effects of Bubbles on Turbulent Flows in Vertical Channels. 7th *Int. Conf. Multiphase Flow*, Tampa, FL, 2010.

[39] Philip J, Marusic I, Large-scale eddies and their role in entrainment in turbulent jets and wakes. *Phys. Fluids* 24:055108-1-10, 2012.

[40] Sunol F, Gonzalez-Cinca R, Rise, bouncing and coalescence of bubbles impacting at a free surface. *Colloids Surf.* A 365: 36-42, 2010

[41] Marucci G, A theory of coalescence. *Chemical Eng. Sci*. 24: 975-985, 1969